

Response of Tropical Deep Convection to Localized Heating Perturbations: Implications for Aerosol-Induced Convective Invigoration

HUGH MORRISON AND WOJCIECH W. GRABOWSKI

National Center for Atmospheric Research, Boulder, Colorado*

(Manuscript received 31 January 2013, in final form 24 May 2013)

ABSTRACT

A cloud-system-resolving model is used to investigate the effects of localized heating/cooling perturbations on tropical deep convection, in the context of the aerosol “invigoration effect.” This effect supposes that a reduction of droplet collision–coalescence in polluted conditions leads to lofting of cloud water in convective updrafts and enhanced freezing, latent heating, and buoyancy. To specifically isolate and test this mechanism, heating perturbations were applied to updrafts with corresponding cooling applied in downdrafts. Ensemble simulations were run with either perturbed or unperturbed conditions and large-scale forcing from a 7.5-day period of active monsoon conditions during the 2006 Tropical Warm Pool–International Cloud Experiment. In the perturbed simulations there was an initial invigoration of convective updrafts and surface precipitation, but convection returned to its unperturbed state after about 24 h because of feedback with the larger-scale environment. This feedback led to an increase in the horizontally averaged mid-/upper-tropospheric temperature of about 1 K relative to unperturbed simulations. When perturbed conditions were applied to only part of the domain, gravity waves rapidly dispersed buoyancy anomalies in the perturbed region to the rest of the domain, allowing convective invigoration from the heating perturbations to be sustained over the entire simulation period. This was associated with a mean mesoscale circulation consisting of ascent (descent) at mid-/upper levels in the perturbed (unperturbed) region. In contrast to recent studies, it is concluded that the invigoration effect is intimately coupled with larger-scale dynamics through a two-way feedback, and in the absence of alterations in the larger-scale circulation there is limited invigoration beyond the convective adjustment time scale.

1. Introduction

Different modeling studies have indicated a wide range of the response of deep convection to aerosol loading (Tao et al. 2007, their Table 5; Tao et al. 2012, their Table 4). Nonetheless, there is agreement among several studies that invigoration occurs in polluted conditions, especially under conditions of weak vertical wind shear in the environment (e.g., Koren et al. 2005; Khain et al. 2005; van den Heever et al. 2006; Seifert and Beheng 2006; Tao et al. 2007; Rosenfeld et al. 2008, hereafter R08; Lee et al. 2008; Fan et al. 2009; Khain and Lynn 2009; Lebo and Seinfeld 2011; Ekman et al. 2011; Lee 2012; Fan et al. 2012a,b; Storer and van den Heever 2013). Many of

these studies have attributed such invigoration to increased latent heating and buoyancy associated with delayed warm-rain formation (droplet collision–coalescence) in polluted conditions and hence greater lofting of cloud water and its subsequent freezing and intensification of ice processes above the 0°C level (e.g., Khain et al. 2005; Seifert and Beheng 2006; R08; Lebo and Seinfeld 2011; Ekman et al. 2011; Fan et al. 2012a,b). R08, Lee (2012), and Fan et al. (2012b) suggested that these changes in heating in turn affect larger-scale circulations.

A key point is that the studies cited above modeled individual clouds or cloud systems using relatively short integrations (a few days or less, and often only a few hours). While these studies have advanced our understanding of interactions between aerosols, cloud microphysics, and convective dynamics, they are less applicable to studying the response of deep convection over larger spatiotemporal scales. This is because such simulations neglect dynamic and thermodynamic feedbacks between convection and its larger-scale environment. Such feedbacks exert a dominant control on convective characteristics in

*The National Center for Atmospheric Research is sponsored by the National Science Foundation.

Corresponding author address: Hugh Morrison, National Center for Atmospheric Research, 3450 Mitchell Lane, Boulder, CO 80307.
E-mail: morrison@ucar.edu

many regimes—tropical convection, in particular (Emanuel 1994).

To investigate the longer-time-scale convective response to aerosol loading, Grabowski (2006, hereafter G06) and Grabowski and Morrison (2011, hereafter GM11) simulated aerosol effects in convective–radiative quasi equilibrium (CRQE), assuming a fixed sea surface temperature (SST). CRQE is arguably the simplest framework for investigating feedbacks between convection and the larger-scale environment. In contrast to previous studies on the short-time-scale response of clouds to aerosols, G06 and GM11 found almost no impact on domain-mean surface precipitation. This occurred because in CRQE, surface precipitation is constrained by radiative cooling of the atmosphere and the surface Bowen ratio (ratio of sensible and latent heat fluxes) through the bulk water and moist static energy budgets, neither of which was strongly affected by aerosols. Van den Heever et al. (2011) and Storer and van den Heever (2013) extended these studies by examining aerosol effects in CRQE using a large domain ($\sim 10^4$ versus 100–200 km in G06 and GM11). They also found little impact on domain-mean surface precipitation. However, the large domain in their simulations allowed for larger-scale organization of deep convection into moist and dry bands. Results indicated enhanced circulations between the dry and moist bands in polluted relative to pristine conditions, with enhanced precipitation and convective mass flux within moist bands in polluted conditions, but a reduction of light precipitation associated with shallower clouds elsewhere.

Other recent studies have simulated aerosol indirect effects in deep convective regimes over large spatiotemporal scales, but with large-scale forcing from observations or analyses instead of CRQE. Lee et al. (2012) found that an initial aerosol perturbation can affect cloud and precipitation characteristics for a period of time after the perturbation is removed because of feedback with the larger-scale environment (we note that they examined precipitating shallow convection rather than deep convection). Seifert et al. (2012) showed that aerosols can have a large impact on local, instantaneous precipitation, but effects were very small when averaged over time and space. They suggested that the small impact of aerosols on average precipitation was a result of feedbacks with mesoscale dynamics that buffer these effects. Morrison and Grabowski (2011, hereafter MG11) also found small impacts on precipitation in 7.5-day simulations of active monsoon conditions during the Tropical Western Pacific–International Cloud Experiment (TWP-ICE). They noted that precipitation was strongly constrained by the observationally derived large-scale forcing. They also showed a slight weakening of convection in polluted conditions,

which is in contrast with studies supporting convective invigoration. This occurred because of adjustment and feedback between convection and its larger-scale thermodynamic environment, with polluted conditions leading to thicker anvil clouds containing smaller ice crystals and consequently to increased upper-tropospheric radiative heating and stabilization.

More generally, the importance of convective feedback and adjustment in controlling the response of deep convection to perturbed conditions has been investigated by several previous studies. Tompkins and Craig (1998) found that a new quasi-equilibrium state was reached over a period of about 15 days following an SST perturbation applied in CRQE. They describe two time scales of adjustment: a longer period (approximately a few weeks) related to the balance between radiative cooling and large-scale subsidence and a shorter adjustment period (<4 days) governed by the convective mass flux. Cohen and Craig (2004) also describe rapid (~ 1 h) adjustment to changes in large-scale tropospheric cooling occurring through gravity wave propagation between convective cells, similar to the mechanism proposed by Bretherton and Smolarkiewicz (1989). Mapes (2004) examined the convective response of nudging to horizontally uniform heating/cooling and moistening/drying perturbations, including parameterized feedback with large-scale vertical motion, and found a near-linear response of the surface rain rate. Tulich and Mapes (2010), Kuang (2010), and Nie and Kuang (2012) studied the transient response of convection to instantaneous, short-lived (10 min), or time-invariant horizontally uniform static energy and moisture sources. These studies also showed a generally linear response, although it can also be highly stochastic (Tulich and Mapes 2010) and vary between different large-scale forcing regimes (Kuang 2010).

Despite the relevance of these studies to the response of deep convection from aerosol perturbations, there has been little study of aerosol indirect effects in the context of convective adjustment. To address this gap, we examine in detail convective adjustment that occurs from applying localized heating perturbations that represent the response to an increase in aerosol loading following the “convective invigoration” mechanism of R08 and others (we will refer to the convective invigoration effect of aerosols as that which is specifically associated with latent heating changes in updrafts and downdrafts). Our broad goal is to bridge previous studies showing significant aerosol effects on deep convection over short time scales with studies showing much smaller impacts over longer time scales. Herein, we examine convective adjustment to perturbed conditions in 7.5-day simulations of TWP-ICE using a model setup

similar to MG11. However, in contrast to MG11 we apply idealized heating perturbations to isolate the convective invigoration effect of aerosols associated with increased latent heating in convective updrafts in polluted conditions. Time-evolving large-scale forcing derived from observations (Xie et al. 2010) is employed. This allows us to study convective adjustment under realistic large-scale forcing representing active monsoon conditions and provides consistency with previous studies of aerosol impacts on deep convection for TWP-ICE (Lee and Feingold 2010; MG11; Lee 2012).

To specifically test the convective invigoration effect, we perform sensitivity tests with heating perturbations applied to convective updrafts above the freezing level to mimic the impact of enhanced freezing and ice processes on latent heating in polluted conditions. Unlike previous studies investigating the convective response to horizontally uniform static energy and moisture perturbations (Mapes 2004; Tulich and Mapes 2010; Kuang 2010; Nie and Kuang 2012), we apply heating perturbations in updrafts and cooling in downdrafts so as to give no net change in moist static energy (as discussed in section 3, net moist static energy cannot change by the convective invigoration effect of aerosols alone over time scales longer than the lifetime of individual convective storms). Hence, horizontal convective-scale buoyancy gradients are directly enhanced in these simulations, all else being equal, while domain-mean column moist static energy is unaltered. The key point is that this allows for an unambiguous evaluation of the impact of convective-scale heating perturbations following the mechanism of R08 in the context of feedback and adjustment with the larger-scale environment. It has been very difficult to isolate effects of perturbed heating associated with the aerosol invigoration effect in previous studies because of the myriad microphysical and dynamical processes that are also altered with perturbations to aerosols (cf. Morrison 2012). The simplified framework in the current study addresses this difficulty and allows for a more systematic investigation of the invigoration effect. We note that there are many other interactions between aerosols, microphysics, and dynamics that could potentially result in invigoration (or weakening) of deep convection, such as impacts on cold pools and low-level convergence (e.g., Lee et al. 2008), condensate loading (e.g., Storer and van den Heever 2013), and changes in ice particle size and hence radiative heating rates within anvils (e.g., MG11). However, the goal of this study is to specifically focus on the convective invigoration effect associated with enhanced latent heating, which is arguably the most widely cited mechanism for invigoration of deep convection [e.g., see discussions in R08 and Fan et al. (2012b)].

2. Model description

The dynamic model is the same as used in G06, GM11, and MG11. It is a two-dimensional (2D), nonhydrostatic anelastic fluid flow model that was also used as the “superparameterization” in simulations described in Grabowski and Smolarkiewicz (1999) and Grabowski (2001, 2004). Horizontal grid spacing is 1 km with a horizontal domain extent of either 200 or 1000 km; sensitivity of TWP-ICE simulations to horizontal grid spacing and domain size is further detailed in MG11. Specifically, there was little sensitivity of results to a decrease of horizontal grid spacing from 1 to 500 km and an increase in the domain size from 200 to 600 km. Furthermore, as will be shown, results for the 1000-km domain are consistent with the 200-km domain when heating/cooling perturbations are applied to the entire domain. Note that the large-scale forcing is based on an observational network with an approximate scale of about 200 km, but we keep the same forcing for the large-domain simulations as in Lee (2012) to allow a direct comparison of simulations with different domain sizes. The model applies 97 vertical levels over a stretched grid, with a model top at 25 km. Surface latent and sensible heat fluxes and horizontal momentum fluxes are calculated using Monin–Obukhov similarity and a nonlocal boundary layer scheme (e.g., Troen and Mahrt 1986) is applied to represent unresolved transport within the boundary layer.

A description of the microphysics parameterization is given by MG11 and references therein. The warm-rain scheme is the two-moment bulk scheme of Morrison and Grabowski (2007, 2008a). Ice processes are represented using the two-moment, three-variable scheme of Morrison and Grabowski (2008b). This scheme allows variable rime mass fraction based on separate prediction of the ice mixing ratios grown by vapor deposition and riming. The radiative transfer model comes from the National Center for Atmospheric Research (NCAR)’s Community Climate System Model (Kiehl et al. 1994), with coupling of microphysics and radiation described by MG11. Aerosol conditions are given by the three-mode lognormal aerosol size distribution for pristine conditions described in MG11. Size distribution parameters for the modes of 0.03, 0.18, and 4.4 μm for the mean radius and standard deviations of 1.12, 1.45, and 1.8 μm are specified as typical of active monsoon conditions based on Allen et al. (2008). Total aerosol concentration is 354.4 cm^{-3} , partitioned into the three modes as 259, 95, and 0.4 cm^{-3} (from smallest to largest mode), which is similar to relatively pristine conditions observed on 6 February (Allen et al. 2008). To isolate the effect of heating/cooling perturbations on convection, we apply these perturbations directly in simulations and do not vary aerosol properties.

3. Case description and experimental setup

To explore interactions between convection and the larger-scale environment in the context of the convective invigoration effect, we simulate a 7.5-day period of active monsoon conditions during TWP-ICE using a model setup similar to that of MG11 and Fridlind et al. (2012). TWP-ICE took place in the vicinity of Darwin, Australia, from 20 January to 13 February 2006 (May et al. 2008). The TWP-ICE domain consisted of several ground sites that gathered precipitation, meteorological, and surface flux measurements, and was centered on a heavily instrumented site operated by the U.S. Department of Energy Atmospheric Radiation Measurement Program (ARM) and Australian Bureau of Meteorology that included cloud and scanning weather radars. The domain was surrounded by an array of five 3-hourly soundings. A detailed comparison of the model with TWP-ICE observations is given by MG11 and Fridlind et al. (2012) and hence is not described here.

The model setup is similar to that for the ARM Global Energy and Water Cycle Experiment (GEWEX) Cloud System Study (GCSS) cloud model intercomparison (Fridlind et al. 2012). Large-scale horizontal and vertical advective forcings of water vapor q and potential temperature θ are derived from observations (Xie et al. 2010). These forcings are modified above 13 km to minimize drift in simulated profiles using an approach similar to Fridlind et al. (2012). We emphasize that the applied large-scale advective forcings are identical in all simulations. Large-scale vertical advection of the prognostic cloud quantities is calculated using the specified large-scale vertical velocity and modeled quantities, while large-scale horizontal advection of cloud quantities is neglected. Initial conditions (θ , q) are derived from sounding observations (Xie et al. 2010). Random perturbations with a maximum amplitude of ± 0.25 K are applied to the θ field between heights of about 100 and 600 m every 30 min to represent underresolved boundary layer heterogeneity. The simulated period is from 0000 UTC 18 January to 1200 UTC 25 January.

To simplify the analysis, especially for mesoscale circulations that develop when perturbed conditions are only applied to part of the domain in the large domain simulations, we follow an approach similar to Lee (2012) and nudge the horizontally averaged u wind above 500 m to 0 m s^{-1} with a nudging time scale of 2 h. However, because surface heat fluxes are strongly dependent upon the magnitude of the low-level wind, we specify surface sensible and latent heat fluxes based on a simulation using nudging of the horizontally averaged winds toward observations (identical to the model configuration in MG11). Specification of the surface heat fluxes is identical in all

simulations shown here; thus, our study neglects feedbacks between surface heat fluxes and strength of convection. While large-scale shear may be expected to have an impact on the convective characteristics, additional simulations with nudging of the horizontally averaged u wind toward observations of Xie et al. (2010), identical to the model configuration used in MG11, show limited sensitivity. For example, time-averaged profiles of horizontally averaged updraft mass flux, fraction of the domain with convective updrafts (defined using a threshold vertical velocity of 1 m s^{-1}), and radiative heating rate, among other quantities, generally vary less than 5%–10% between simulations with nudging of the u wind toward observations versus zero wind.

Because of the relatively limited predictability of moist deep convection and rapid growth of small perturbations at convective scales (e.g., Tan et al. 2004; Zhang et al. 2007; MG11), we employ an ensemble approach to contrast significant differences between simulations from noise. Following MG11, we use 240 and 120 ensemble members for the small (200 km)- and large (1000 km)-domain simulations, respectively. Different ensemble members are generated by using different random number seeds for the applied low-level θ perturbations. Large spread of horizontally averaged convective characteristics among ensemble members occurs at any given time. However, ensemble spread is much smaller for time-averaged convective characteristics. For example, time- and horizontally averaged vertical profiles of updraft mass flux and convective updraft fraction within the domain vary by less than 15% and 20%, respectively, among ensemble members for the baseline configuration below 10 km, with somewhat larger spread above 10 km. Moreover, ensemble spread is similar among all model configurations, including the baseline and all sensitivity simulations described herein. All presented results are ensemble averaged; a more detailed discussion of spread among ensemble members is given by MG11.

To specifically test the convective invigoration mechanism proposed by R08 and others, whereby enhanced freezing and latent heating in updrafts lead to an increase in buoyancy in polluted conditions, we apply perturbed heating in updrafts and cooling in downdrafts. These heating and cooling perturbations are consistent with differences in latent heating between pristine and polluted conditions in individual convective storms found by previous bin model studies (e.g., Khain et al. 2005; Lebo and Seinfeld 2011; Fan et al. 2012b). In our simulations, all other aspects are identical to the baseline simulation (BASE) to isolate the impact of convective-scale heating perturbations. Perturbed heating is applied to updrafts, with the amplitude of the perturbation a function of the local latent heating rate.

TABLE 1. List of model experiments.

Name	Description	Perturbations applied to PART or ALL of the domain	Domain length (km)
BASE	No heating/cooling perturbations applied	—	200
PERT	Latent heating increased by a factor of 1.2, corresponding cooling applied in downdrafts; perturbations applied over the entire duration of the simulations	ALL	200
PERT0.7	As in PERT, but latent heating decreased by a factor of 0.7	ALL	200
PERT1.1	As in PERT, but latent heating increased by a factor of 1.1	ALL	200
PERT1.3	As in PERT, but latent heating increased by a factor of 1.3	ALL	200
PERTL	As in PERT, but 1000-km domain	ALL	1000
PERTD	As in PERT, but perturbed heating and cooling only applied after 0000 UTC 19 Jan	ALL	200
PERTE	As in PERT, but perturbed heating and cooling stopped after 0000 UTC 21 Jan	ALL	200
PERTP	As in PERT, but perturbed heating and cooling only applied to the inner 250 km of the 1000-km domain	PART	1000

Perturbed cooling is applied in downdrafts at a rate that exactly balances the perturbed heating in updrafts, such that the domain-total moist static energy is unchanged. This is an important point, as any imbalance in the domain-total heating and cooling rates would represent a net source or sink and, hence, forcing of moist static energy, which is not possible through the convective invigoration effect alone over time scales longer than a few hours. This is explained as follows. Enhanced freezing induced by aerosols from the convective invigoration effect can increase the net moist static energy over short time scales. However, the increased amount of ice must eventually either sublimate or melt, which implies no net change in domain-total moist static energy over time scales longer than the lifetime of individual storms (a few hours). Given that the domain at any given time consists of a number of individual cells at various stages in their life cycle, it is reasonable to assume an exact balance in the source of moist static energy through freezing and the sink through melting or sublimation for the domain as a whole. The perturbed heating and cooling is applied between heights of 6 and 8 km (roughly 1–3 km above the freezing level), although vertical advection leads to a separation and a dipole structure of net heating above cooling. Applying heating and cooling perturbations at the same level represents a simplification, but this assumption is supported by bin model simulations of the convective invigoration effect (Khain et al. 2005, their Figs. 7, 8, and 10). We also note that direct or indirect aerosol effects on radiation can produce a net source or sink of moist static energy, but in this paper we are concerned only with aerosol indirect effects via enhanced latent heating/cooling.

Except as noted, heating/cooling perturbations are applied at the start of the simulations, and they continue for the duration of the simulations. We note that convection is initially in a state of imbalance with the rate

of tropospheric destabilization from large-scale forcing, radiative cooling, and surface fluxes, leading to rapid CAPE consumption once convection is initiated after the first few hours of integration. Previous studies of convective adjustment with perturbed conditions have generally allowed the model to first reach quasi equilibrium with the large-scale forcing before applying the perturbation (e.g., Tompkins and Craig 1998; Cohen and Craig 2004; Mapes 2004; Tulich and Mapes 2010). However, here we have chosen to begin applying perturbed conditions at the initial time since this is the approach used in nearly all CRM simulations of aerosol effects on convective storms (i.e., perturbed aerosol conditions are applied from the start of the simulation in these studies). Nonetheless, simulations with perturbed conditions only applied after the model has reached quasi equilibrium with the large-scale forcing (after about 24 h) are also described in section 4 to address this issue.

4. Results for perturbed conditions applied to entire domain

A list of all model experiments is provided in Table 1. We first contrast results of simulations with latent heating enhanced by a factor of 1.2 locally in all updrafts across the domain between 6 and 8 km (PERT) with unperturbed simulations (BASE). The local heating rate perturbations applied in the model for PERT are given by

$$Q_H = (c - 1)Q_L, \quad \text{if } w > 0, \quad Q_L > 0, \quad \text{and} \\ 6 \leq z \leq 8 \text{ km}, \quad (1)$$

where Q_L is the local latent heating rate from the model microphysics, $c = 1.2$ is the latent heating enhancement factor, w is the vertical velocity, and z is height. A local cooling rate perturbation is applied when $w < 0$ such

that the horizontal average balances the heating perturbation at each vertical level. The cooling rate perturbations are given by

$$Q_c = \langle Q_H \rangle \frac{A_H}{A_C}, \quad \text{if } w < 0 \quad \text{and} \quad 6 \leq z \leq 8 \text{ km}, \quad (2)$$

where A_H and A_C are the horizontal extents of the heating and cooling areas, respectively, at a given level within the domain, and angle brackets indicate a horizontal average over A_H . For simplicity, the same perturbed cooling rate is applied to all grid points with $w < 0$ at a given level (i.e., perturbed cooling in downdrafts is not a function of downdraft strength or latent cooling rate). For PERT, $c = 1.2$ is comparable to differences in latent heating between pristine and polluted conditions in previous CRM simulations (Khain et al. 2005; Lebo and Seinfeld 2011; Fan et al. 2012b). In particular, Fan et al. (2012b) show an increase in latent heating rate of 10%–20% in the mid- and upper troposphere in polluted compared to pristine conditions because of the convective invigoration effect (over approximately a 1-day time scale); thus, our enhancement is consistent with the upper range from their study. Tests with different perturbation amplitudes are described later in the section (see also Table 1).

Note that the heating perturbation is proportional to the local latent heating rate from the microphysics as expressed in (1), and hence is approximately proportional to updraft velocity in supersaturated conditions. This is a key point, because the amplitude of the applied heating perturbation will therefore be greater for strong compared to weak updrafts. A linear dependence of heating perturbation on the latent heating rate, and hence approximately linear dependence on vertical velocity, is reasonable since the convective invigoration mechanism relies primarily on lofting of cloud water above the freezing level leading to enhanced freezing and ice processes; in the absence of entrainment and precipitation, the upward liquid water flux at a given height will be proportional to updraft velocity. Entrainment and precipitation will modify this picture, but in ways that are not clearly understood.

We also note that enhancement of latent heating associated with the invigoration effect may vary over the life cycle of individual storms. For example, the simulations of Storer and van den Heever (2013) showed greater enhancement of latent heating earlier in the storm lifetime. In the simulations here there are storms in various stages of their life cycle at any given time when considering the ensemble members together, so any life-cycle effect is expected to be limited when analyzing the ensemble mean. Thus, for simplicity we assume that c is constant.

All else equal, increased heating in updrafts and cooling in downdrafts in PERT leads to increased convective-scale buoyancy gradients and stronger convective updrafts and downdrafts compared to BASE. This produces an initial invigoration of convection evident in time series of average updraft mass flux M_u , average convective updraft mass flux M_c , and fraction of the domain with convective updrafts F_c at a height of 9.5 km (for reference, the mean height of anvil top is about 18 km in BASE and PERT), once deep convection initiates approximately 2.5 h into the simulations (Fig. 1). Here, grid points with convective updrafts are defined as those with $w \geq 1 \text{ m s}^{-1}$. We define M_c as the mass flux conditionally averaged over points with $w \geq 1 \text{ m s}^{-1}$. There is also a small increase in horizontally averaged surface precipitation (PRE) associated with the initial convective invigoration (Fig. 1e). To better illustrate the initial invigoration, Fig. 2 shows the same quantities in Fig. 1 but only during the first 36 h of the simulations.

A key point is that the larger-scale environment quickly responds (within less than 1 h after convective initiation) to the enhanced convection in PERT, which is illustrated by time series of horizontally averaged temperature \bar{T} at a height of 9.5 km (Figs. 1d and 2d). Increased \bar{T} in the mid- and upper troposphere in PERT relative to BASE results in stabilization; hence, convective invigoration is reduced over time and M_u , M_c , F_c , and PRE in PERT approach values from BASE within approximately the first 24 h. Thereafter, PERT and BASE produce almost identical convective characteristics, with a close balance between the perturbed heating in updrafts and cooling in downdrafts and increased stability resulting from the roughly 1-K increase in mid- and upper-tropospheric \bar{T} in PERT. Interestingly, despite the fact that the amplitude of the applied heating perturbations is greater for strong compared to weak updrafts as described above, there is almost no difference in the distribution of convective updraft strength between PERT and BASE at a given vertical level (Fig. 3). As described later, if we stop applying the heating/cooling perturbations during the simulations, the mid- and upper-tropospheric \bar{T} reverts back to that of BASE over a roughly 1-day time scale.

Vertical profiles of \bar{T} , horizontally averaged relative humidity (RH), horizontally averaged radiative heating rate (RAD), M_u , M_c , and F_c , averaged between 1200 UTC 19 January and 1200 UTC 25 January (i.e., after adjustment of the larger-scale environment), are shown in Fig. 4. The similarity of convective characteristics between PERT and BASE after the first roughly 24 h is illustrated by profiles of M_u , M_c , and F_c . Profiles of cloud microphysical quantities are also almost identical in PERT and BASE (not shown). Differences in RH and RAD between PERT

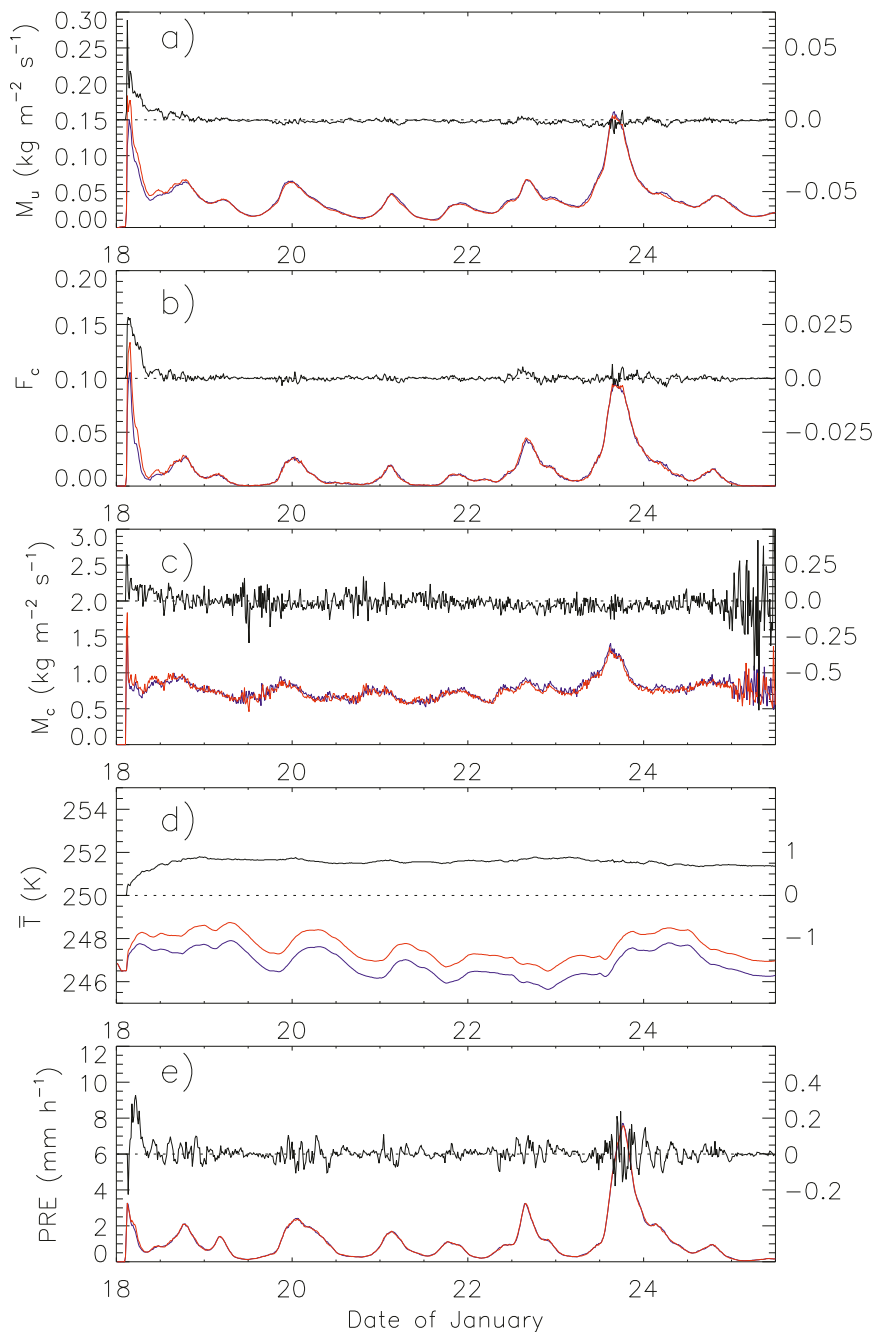


FIG. 1. Time series of (a) horizontally averaged updraft mass flux, (b) fraction of the domain with convective updrafts, (c) convective updraft mass flux, (d) horizontally averaged temperature, and (e) surface precipitation rate for the perturbed (PERT) (red) and unperturbed (BASE) (blue) simulations. The terms in (a)–(d) are all shown at a height of 9.5 km. Black solid lines indicate differences (PERT minus BASE), with black dotted lines included as a reference to show zero difference.

and BASE are also small. The increase in \bar{T} of about 1 K in PERT compared to BASE is fairly uniform between about 7.5 and 20 km. Also, \bar{T} is slightly lower in PERT from the surface to about 6 km, which is associated with downward

transport of cold perturbations in downdrafts to below the level at which cooling is applied.

The increase in \bar{T} above 6 km in PERT compared to BASE is associated with two processes. First, there is

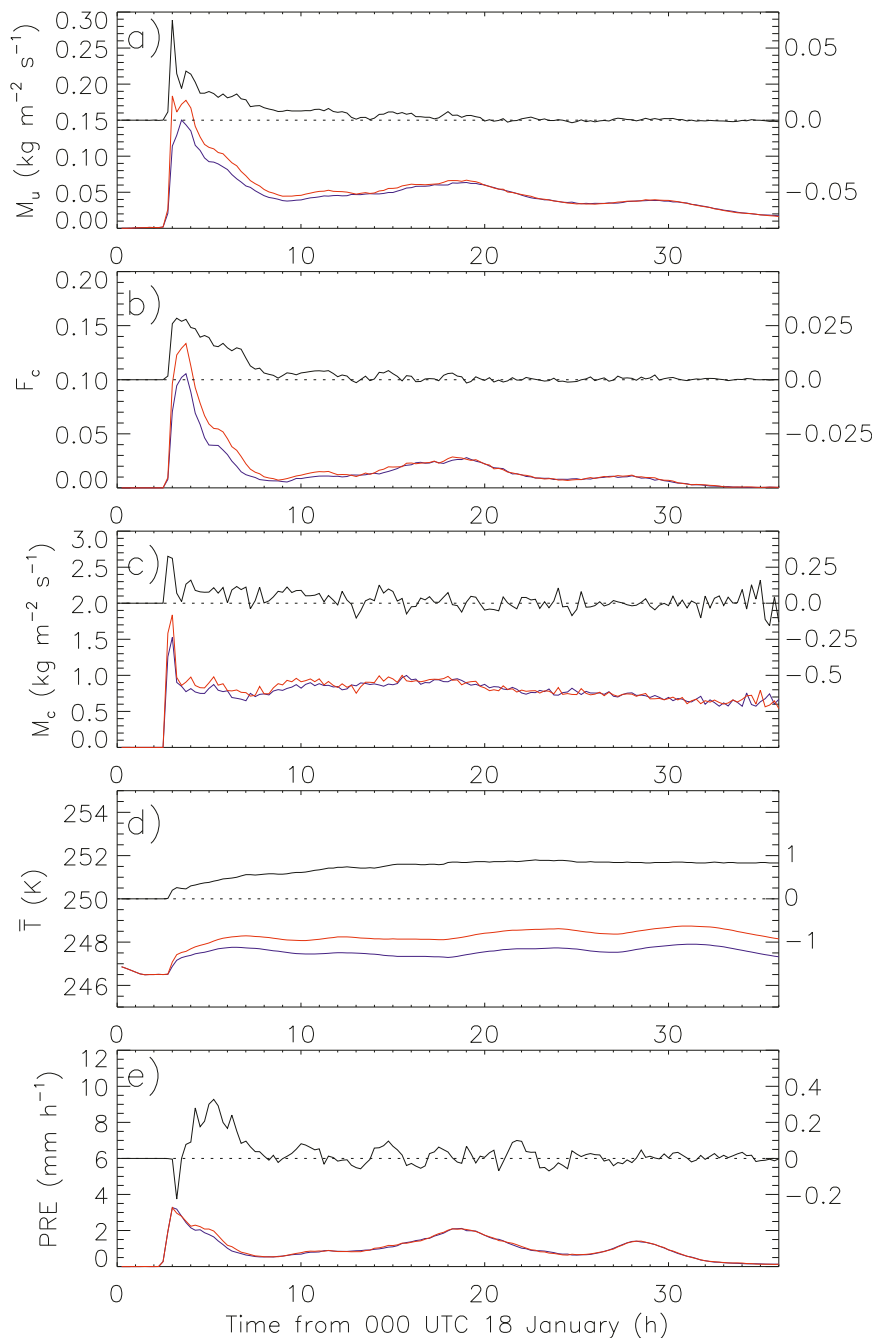


FIG. 2. As in Fig. 1, but for the first 36 h of the simulations.

greater net latent heating associated with greater PRE during the adjustment period in PERT (Figs. 1e and 2e). Second, there is net warming above 6 km directly associated with the applied heating perturbation and subsequent upward warm advection in updrafts. The latter contribution is exactly balanced by the small reduction of \bar{T} associated with the applied cooling when $w < 0$ and subsequent cold advection below 6 km. We estimate the

contribution of increased net latent heating (PRE) to the increase in \bar{T} above 6 km in PERT by comparing the total difference in PRE between PERT and BASE integrated over the simulation period ($2.53 \times 10^6 \text{ J m}^{-2}$) to the difference in vertically integrated, horizontally averaged dry static energy above 6 km (the height above which PERT is warmer than BASE) at the end of the simulations ($5.98 \times 10^6 \text{ J m}^{-2}$). This gives an estimated

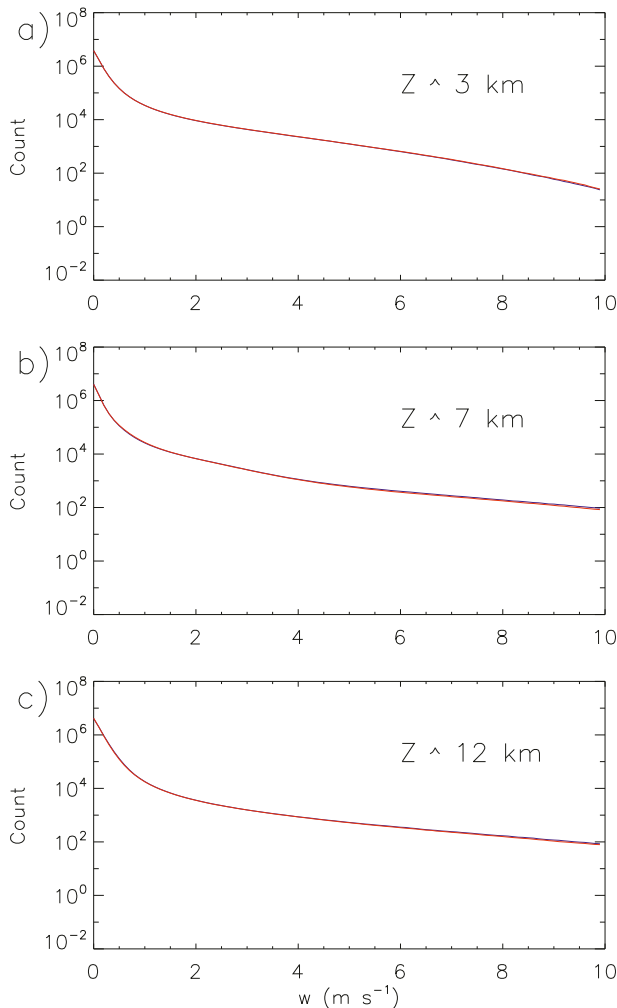


FIG. 3. Histograms of updraft velocity for the PERT (red) and BASE (blue) simulations for approximate heights of (a) 3, (b) 7, and (c) 12 km. Shown are ensemble-averaged total counts in evenly spaced vertical velocity bins of width 0.1 m s^{-1} , calculated over the last 6 days of the simulations (between 1200 UTC 19 Jan and 1200 UTC 25 Jan).

contribution of 42% for the difference in latent heating associated with surface precipitation to the total increase in \bar{T} above 6 km, with the remaining increase associated directly with the applied heating perturbations. This suggests that both vertical advection of warm/cold perturbations and increased net latent heating associated with greater PRE are important in explaining the response of \bar{T} in PERT.

Closer inspection of the time series of M_w , M_c , F_c , and \bar{T} at 9.5 km during the adjustment period over the first 36 h of integration (Figs. 2a–d) reveals some interesting features. Once convection begins around 0230 UTC 18 January, there is a rapid rise in mid- and upper-tropospheric \bar{T} in both PERT and BASE within the first

hour, but the increase is much larger in PERT. Thereafter, there is a slower increase in \bar{T} over the next roughly 16 h in PERT while convective characteristics (i.e., F_c and M_c) converge to BASE.

In general, convective adjustment involves several processes that interact in complex ways and hence many time scales (e.g., Tompkins and Craig 1998; Cohen and Craig 2004; Kuang 2010). For example, Kuang (2010) constructed linear response functions to temperature and moisture perturbations and found a range of time scales depending on the vertical structure of the perturbations; physical interpretation of the time scales is nontrivial. However, a key difference between our simulations and those of Kuang (2010) is that here the perturbations are applied within updrafts with an amplitude that is a function of the local latent heating rate, while Kuang (2010) applied time-invariant and horizontally homogeneous perturbations. While recognizing the possibility that many processes may be involved in the adjustment, it is reasonable to think that convective vertical mixing is critical here since the amplitude of the applied heating perturbations are a function of the local latent heating rate that in turn depends on the convective vertical velocity itself. In other words, in order to realize the heating perturbations air parcels must be transported by updrafts through the 6–8-km level. Moreover, previous studies have shown the importance of gravity waves in controlling the adjustment of the environment to heating in clear air surrounding cumulus clouds (e.g., Bretherton and Smolarkiewicz 1989; Cohen and Craig 2004). Thus, we propose that the adjustment time scale is controlled at least in part by gravity waves and convective vertical mixing as described next.

a. Gravity wave dynamics

Rapid adjustment within the first few hours after convective initiation is consistent with initial convective overturning and adjustment by gravity wave propagation between convective towers. We estimate the gravity wave adjustment time scale τ_{gw} as the ratio of average half-distance between convective towers D_c and the horizontal group velocity C_{gx} similar to Cohen and Craig (2004). They used the hydrostatic Boussinesq equations linearized about the horizontally averaged thermal profile of their simulations to estimate C_{gx} for various vertical modes; a detailed investigation of this sort is beyond the scope of our study. Nonetheless, an estimate is found by assuming a vertical length scale L_z equal to about 10 km [i.e., a full vertical wavelength that is twice the depth of warm anomaly (~ 5 km)]. (It should be kept in mind that the depth of the warm anomaly is greater than the depth of the applied heating perturbations because of vertical advection and additional latent heating

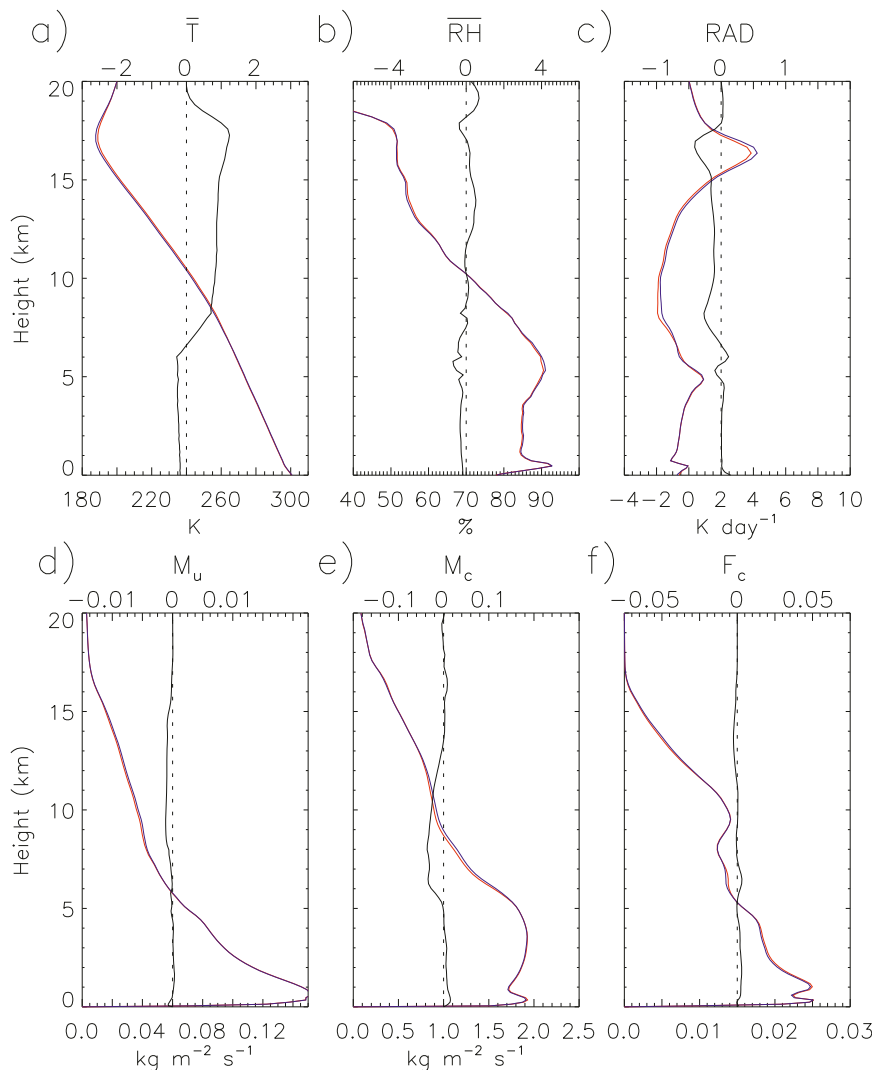


FIG. 4. Vertical profiles of (a) horizontally average temperature, (b) relative humidity, (c) radiative heating rate, (d) domain-average updraft mass flux, (e) domain-average convective updraft mass flux, and (f) fraction of the domain with convective updrafts, averaged between 1200 UTC 19 Jan and 1200 UTC 25 Jan for the perturbed (PERT) (red) and unperturbed (BASE) (blue) simulations. Black solid lines indicate differences (PERT minus BASE), with black dotted lines included as a reference to show zero difference.

associated with stronger updrafts above the level of applied heating.) This gives $C_{gx} \sim 16 \text{ m s}^{-1}$, since $C_{gx} = N/m$ for hydrostatic waves, where N is the mean Brunt-Väisälä (buoyancy) frequency averaged over the troposphere ($\sim 0.01 \text{ s}^{-1}$), and m is the horizontal wavenumber equal to $2\pi/L_z$. Also $D_c = U_d(1 - F_c)/(2F_c)$, where $U_d \sim 10 \text{ km}$ is an estimate of mean updraft diameter. Since $F_c \sim 0.1$ during the initial adjustment period, this gives $D_c \sim 45 \text{ km}$ and hence $\tau_{gw} \sim 1 \text{ h}$. This estimate of τ_{gw} is in agreement with previous studies of gravity wave adjustment in clear air surrounding cumulus clouds (Bretherton and Smolarkiewicz 1989; Cohen

and Craig 2004). Although this likely represents a lower estimate since shallower hydrostatic modes (i.e., larger m) and nonhydrostatic gravity waves have smaller C_{gx} , we note that Bretherton and Smolarkiewicz (1989) found that systematic adjustment in clear air surrounding clouds was still brought about by long-period hydrostatic waves with near-horizontal group velocity.

b. Convective vertical mixing

As discussed above, heating perturbations are applied in updrafts, with an amplitude that depends on the local latent heating rate and hence the convective updraft

mass flux (with corresponding cooling applied in downdrafts). The heating perturbations are therefore realized when air is lifted by updrafts through the 6–8-km level. Thus, it is reasonable to think that convective vertical mixing plays an important role in the adjustment process, which tends to be slower than gravity wave adjustment in clear air surrounding clouds (Bretherton and Smolarkiewicz 1989). We therefore propose that the overall adjustment time scale is also controlled by a convective vertical mixing time scale τ_{cm} , where $\tau_{\text{cm}} \sim L_z/w_c \gg \tau_{\text{gw}}$, which is analogous to a time scale for processing all air within the domain by convective updrafts (i.e., total mass of air in the domain divided by the total convective mass flux within the domain). Here, w_c is a convective vertical velocity scale equal to the product of domain-mean F_c and convective updraft velocity w_u , which is equal to M_c divided by air density ρ . We emphasize that many other time scales may be relevant to the adjustment process but show below that τ_{cm} is consistent with the adjustment time scale seen in the simulations.

During the adjustment period, we estimate $M_c \sim 1 \text{ kg m}^{-2} \text{ s}^{-1}$ and $F_c \sim 0.05$ from the simulations (see Fig. 2). Assuming $\rho \sim 0.5 \text{ kg m}^{-3}$ gives $w_c \sim 0.1 \text{ m s}^{-1}$ and, hence, $\tau_{\text{cm}} \sim 1$ day. This estimate is broadly consistent with the adjustment time scale seen in Fig. 2d. Our estimate of τ_{cm} is somewhat shorter than that reported by Tompkins and Craig (1998), who found a convective mass flux adjustment time scale of about 4 days as a response to SST perturbations in CRQE. An explanation for the relatively short τ_{cm} here is the strength of the large-scale forcing, which produces an order-of-magnitude-larger domain-average convective mass flux (prior to 0600 UTC 18 January) than that associated with the much weaker radiative forcing in the CRQE simulations of Tompkins and Craig (1998). Tompkins and Craig (1998) also described longer time-scale adjustment (~ 15 days) associated with changes in tropospheric radiative cooling and adjustment of water vapor in subsiding air outside of convective updrafts. There is no evidence for longer time-scale adjustment ($\gg 1$ day) to the perturbed conditions in our simulations, which is consistent with our specification of surface fluxes and limited differences in domain-average profiles of RAD (Fig. 4e). Moreover, evolution of the atmospheric state here is strongly driven by the imposed large-scale forcing, which may limit the signal of slow adjustment processes.

Overall, convective adjustment is insensitive to domain size; results for PERTL (simulations as in PERT, except using a 1000-km instead of 200-km domain) are nearly the same as PERT (Fig. 5). We propose that this occurs because adjustment through both gravity wave

dynamics and convective mixing depends upon the relative domain area covered by convective drafts and mean distance between drafts, which are both insensitive to domain size.

In PERT we applied perturbed conditions from the start of the simulations to the end. The initiation of convection within the first few hours of the simulations occurs in strongly nonequilibrium conditions, with a large convective fraction and rapid CAPE depletion prior to the model achieving quasi equilibrium with the applied large-scale forcing. To examine convective adjustment under conditions closer to equilibrium with the large-scale forcing, we apply heating and cooling perturbations as in PERT, but starting only after 0000 UTC 19 January, after 24 h of integration (PERTD). Overall results are similar to PERT, with a rapid period of adjustment within the first few hours after perturbations are applied, followed by slower adjustment as convective characteristics in PERTD approach those of BASE (Fig. 6). After roughly 24 h there is little difference in convective characteristics between PERTD and BASE for the remainder of the simulations (not shown). There are two distinct periods of adjustment in PERTD corresponding to the two periods of convective activity from 0000 to 0900 UTC 19 January and from 1600 to 2400 UTC 19 January. The close correspondence of adjustment with the time series of domain-mean F_c supports our contention that convective vertical mixing has an important influence on the overall adjustment time scale.

Additional simulations were performed in which latent heating/cooling perturbations were applied beginning at the start of the simulations as in PERT, but not applied after 0000 UTC 21 January. In these simulations (PERTE) convection initially weakens after the heating/cooling perturbations are stopped (Fig. 7). This occurs because the environment has been stabilized relative to BASE as a result of adjustment to the heating/cooling perturbations applied earlier, while buoyancy in updrafts is no longer enhanced by the heating perturbations. As a result, there is rapid weakening of convection. The environment subsequently responds to the weakened convection by cooling above about 6 km relative to BASE, and convective characteristics in PERTE approach those of BASE with an adjustment time scale of about 24 h consistent with the previous discussion.

Different perturbation amplitudes were tested by performing additional sets of simulations as in PERT, except with latent heating in updrafts [c in (1)] increased by a factor of either 1.1 or 1.3 (PERT1.1 and PERT1.3, respectively), compared to 1.2 for PERT (consistent modifications were also made to the cooling perturbation in downdrafts so that net moist static energy is unchanged).

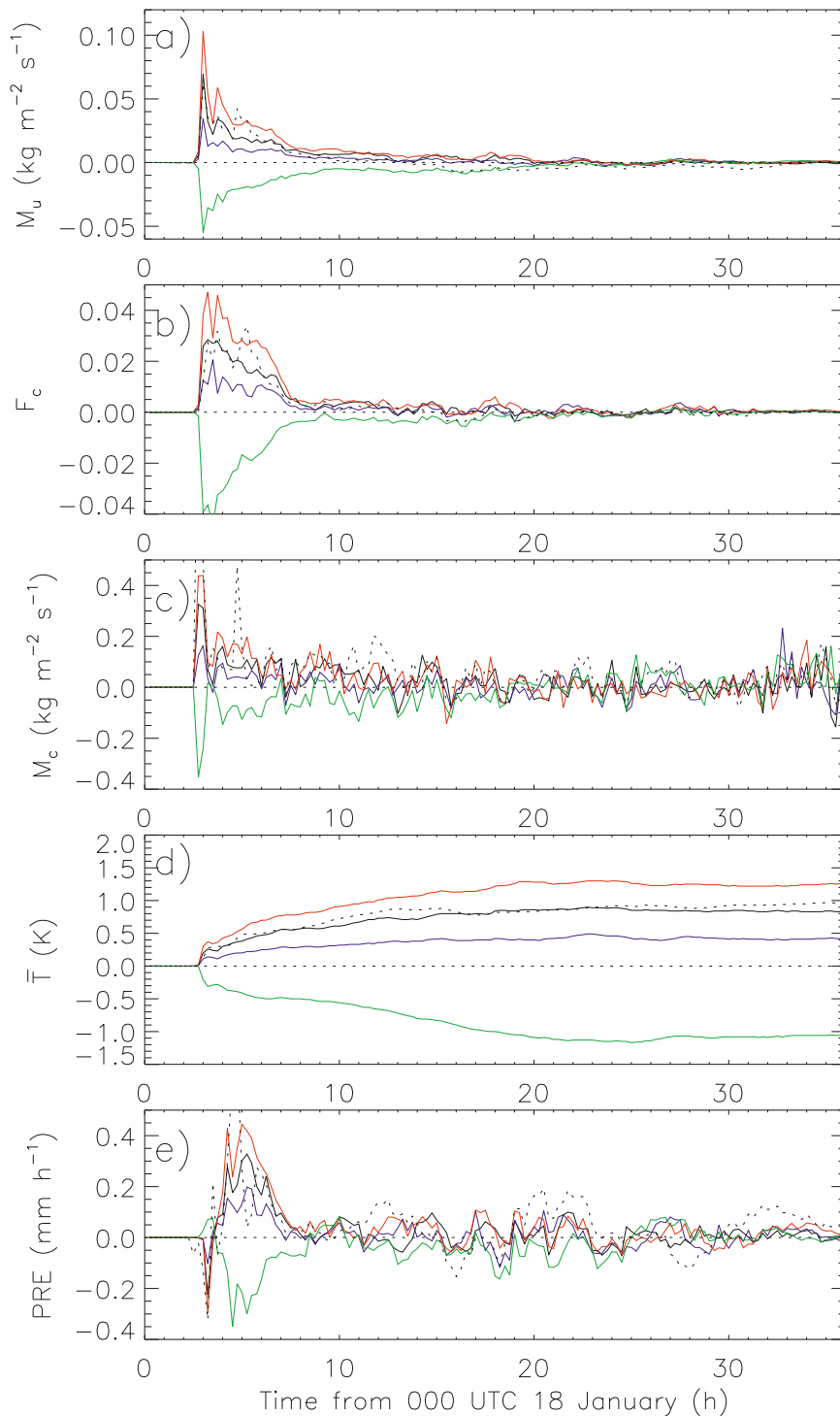


FIG. 5. As in Fig. 1, but time series of differences in various simulations relative to BASE over the first 36 h of the simulations. The simulations presented are PERT (black solid), PERT0.7 (green), PERT1.1 (blue), PERT1.3 (red), and PERTL (black dotted).

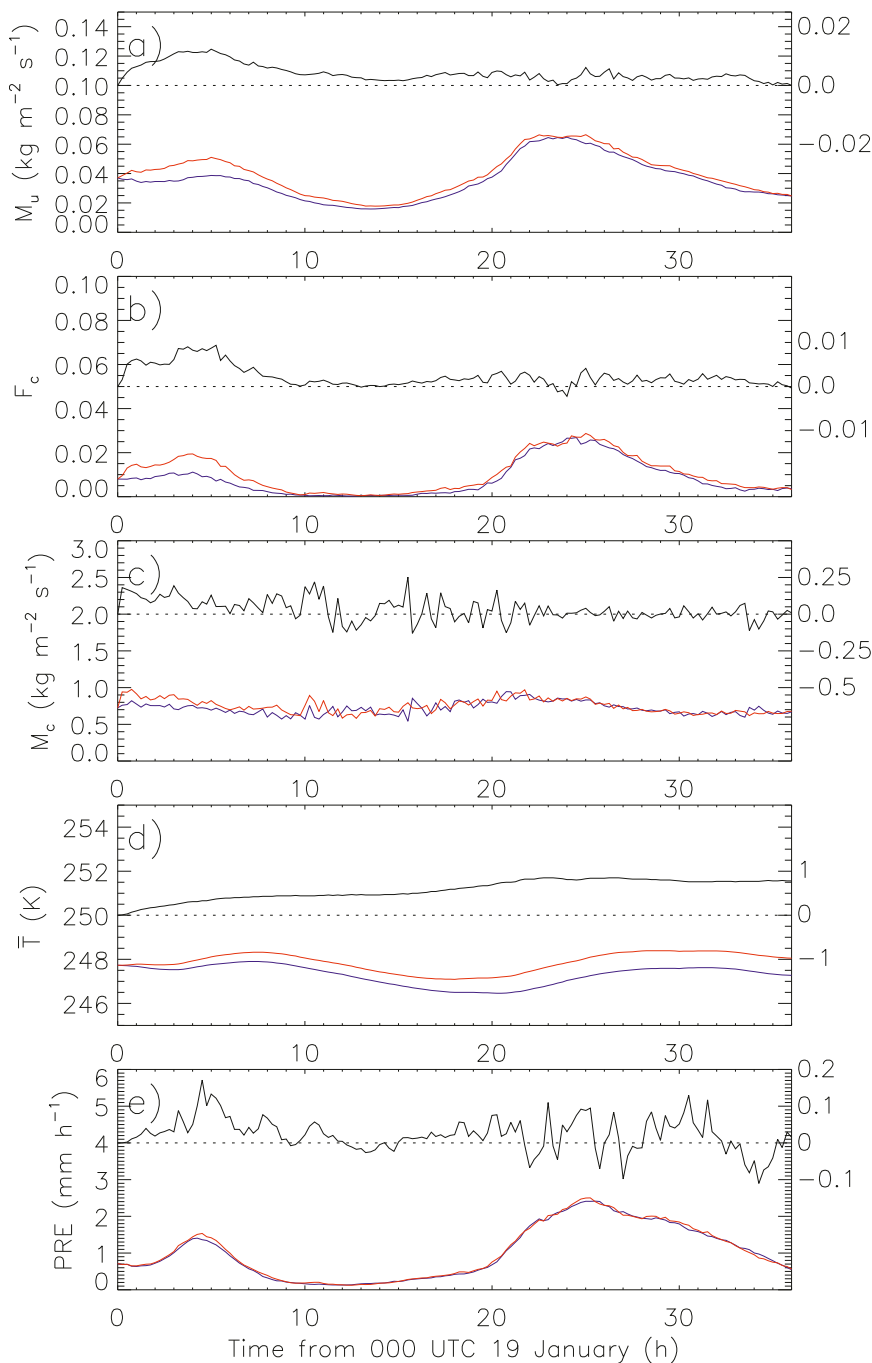


FIG. 6. As in Fig. 1, but for a comparison of PERTD (red) and BASE (blue) over the period from 0000 UTC 19 Jan to 1200 UTC 20 Jan.

A set of simulations with latent heating (cooling) in updrafts (downdrafts) scaled by 0.7 was also tested (PERT0.7). As a whole, the convective response to perturbed heating and cooling is fairly linear with perturbation amplitude, in terms of M_u , F_c , M_c , \bar{T} , and PRE (Fig. 5). A nearly linear convective response was also found by Mapes (2004), Tulich and Mapes (2010), and Kuang (2010) to heating

and cooling perturbations that were applied as horizontal averages across the domain. In contrast to the other experiments, in PERT0.7 there is less heating in updrafts and cooling in downdrafts, leading to an initial weakening of convection and reduction of \bar{T} in the mid- and upper troposphere compared to BASE. Interestingly, the adjustment time scale appears to be mostly independent of

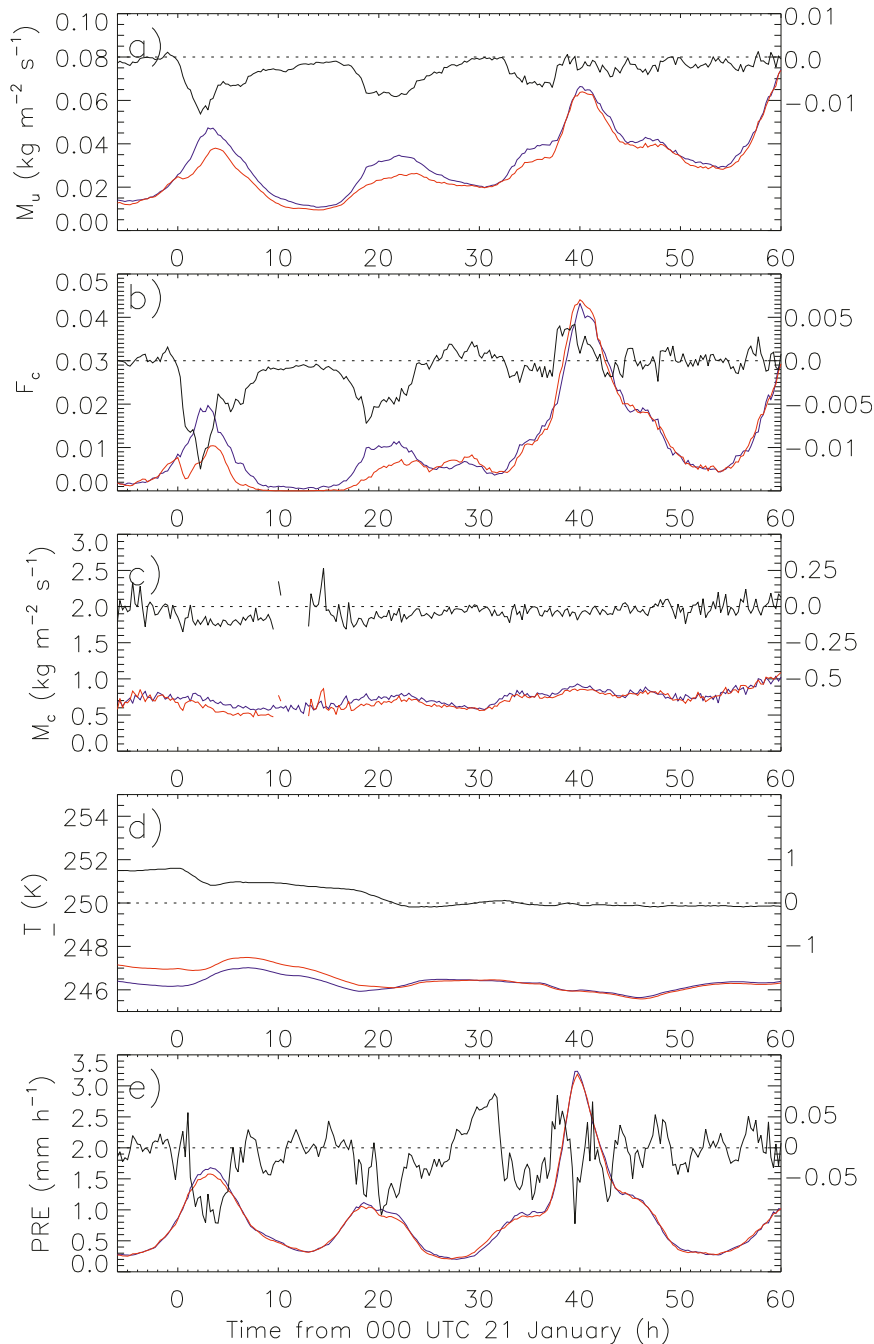


FIG. 7. As in Fig. 1, but for a comparison of PERTE (red) and BASE (blue) over the period from 1800 UTC 20 Jan to 1200 UTC 23 Jan. Note that missing values of M_c for PERTE around 10 h are when there are no convective updrafts in the domain at a height of 9.5 km (i.e., all points at this level have vertical velocities less than 1 m s^{-1}).

the perturbation amplitude. This finding is consistent with the two adjustment processes described above. In particular, the overall values of F_c , M_c , D_c , and N are similar among the simulations, especially after 0700 UTC 18 January. This implies similar τ_{gw} and τ_{wc} among the simulations regardless of the perturbation amplitude.

5. Results for perturbed conditions applied to part of the domain

Significant changes in \bar{T} occur after convective adjustment from applied latent heating and cooling perturbations as described in the previous section. This

implies the potential for mesoscale circulations driven by larger-scale heating gradients if perturbed conditions are only applied to part of the domain. Such mesoscale circulations were previously explored in the modeling study of Lee (2012), who applied aerosol perturbations to part of the domain and found that the aerosol invigoration effect drove a mean circulation between the pristine and polluted parts of the domain. Here, we employ a 1000-km domain and apply perturbed conditions only to the inner 250 km. In these simulations (PERTP), latent heating is increased by a factor of 1.2 in updrafts with compensating cooling in downdrafts, analogous to PERT but only applied within the perturbed part of the domain. In the discussion below we contrast results averaged over the perturbed (PERTURBED) and unperturbed (UNPERTURBED) parts of the domain from these simulations.

There is an initial invigoration of convection in the mid- and upper troposphere in PERTURBED relative to UNPERTURBED (Fig. 8), similar to results with perturbed conditions applied to the entire domain (PERT). However, the invigoration is sustained over the duration of the simulations in contrast to PERT (in which convection returns to its unperturbed state after about 1 day; see section 4). This is also shown by vertical profiles of quantities averaged from 1200 UTC 19 January to 1200 UTC 25 January, revealing that M_c and especially M_u and F_c are larger between about 6 and 16 km for PERTURBED compared to UNPERTURBED (Fig. 9). In contrast to upper levels, there is a weakening of convection in PERTURBED compared to UNPERTURBED below 6 km, evident by profiles of F_c (Fig. 9g). These two primary effects in PERTURBED (i.e., strengthening of convection above 6 km, and weakening below), and impacts on larger-scale circulations, are discussed further below and illustrated in the diagram shown in Fig. 10.

Above 6 km, applying heating perturbations in updrafts drives the initial invigoration of convection in PERTURBED. This leads to an increase in \bar{T} relative to UNPERTURBED because of increased latent heating and vertical advection of warm anomalies in updrafts, similar to PERT. However, in contrast to PERT, the increase of \bar{T} in PERTURBED is limited since any buoyancy anomalies there are rapidly dispersed throughout the rest of the domain by gravity waves (i.e., within a few hours; see discussion in section 4). Thus, differences in \bar{T} between PERTURBED and UNPERTURBED are less than 0.5 K at 9.5 km (Fig. 8d), and much smaller when averaged over time (Fig. 9a), despite mean differences in latent heating rates between these two regions of up to 7 K day^{-1} (Fig. 9h). The key point is that rapid dispersal of buoyancy anomalies in PERTURBED means there is little stabilization of the upper troposphere, in contrast to

PERT. Thus, the applied heating perturbations in updrafts are able to directly drive convective invigoration above 6 km in PERTURBED over the duration of the simulations (Figs. 8 and 9e–g).

The dispersal of diabatic (mostly latent) heating anomalies in the upper troposphere between PERTURBED and UNPERTURBED occurs via gravity waves associated with a mean mesoscale circulation with a spatial scale defined by the size of perturbed and unperturbed regions (250–750 km) and consisting of weak ascent of a few centimeters per second between 8 and 17 km in PERTURBED, with weak descent in UNPERTURBED (Fig. 9d). Note that the increased upward mass flux in PERTURBED associated with invigorated convection and compensating downward mass flux in UNPERTURBED may itself help to drive this mesoscale circulation. However, results suggest this contribution is limited; if the mesoscale circulation was driven directly by the increased upward mass flux in PERTURBED, then the circulation would become established when convection is initially invigorated (i.e., within the first few hours of the simulations) since mass flux compensation associated with mass continuity (required since the model has periodic lateral boundary conditions) is instantaneous. However, the mesoscale circulation does not appear until after about 1.5 days (Figs. 11a, 12a, 13a). Instead, the increased upward mass flux in PERTURBED relative to UNPERTURBED within about the first 1.5 days is mostly balanced by an increased downward mass flux within PERTURBED itself (Figs. 11b,c).

Below 6 km, we propose that the weakening of convection in PERTURBED compared to UNPERTURBED (Fig. 9g) occurs via interactions between latent heating, mesoscale circulation, water vapor, and low-level convection. This is supported by analysis of various quantities averaged over 1.5-day increments (Figs. 11–13). The weakening of convection at low levels does not occur until after several days; F_c is initially larger in PERTURBED relative to UNPERTURBED in both the upper and lower troposphere (Fig. 11f). Within the first 1.5 days, there is a reduction of midlevel (~ 5 km) latent heating associated with enhanced sublimation and melting in PERTURBED (Fig. 11e), because of greater amounts of ice condensate within and above the melting layer (Fig. 9k). As a result, mean mesoscale descent develops below 7 km after 1.5 days in PERTURBED (Fig. 12a), leading to a net transport of dry air from mid- to low levels and, hence, reduction of $\overline{\text{RH}}$ within the boundary layer after 3 days (Fig. 13d). This in turn causes a reduction of low-level moist static energy and hence lower potential energy of convective parcels ascending from the boundary layer. Thus, F_c is smaller in PERTURBED compared to UNPERTURBED below 6 km after roughly 3 days

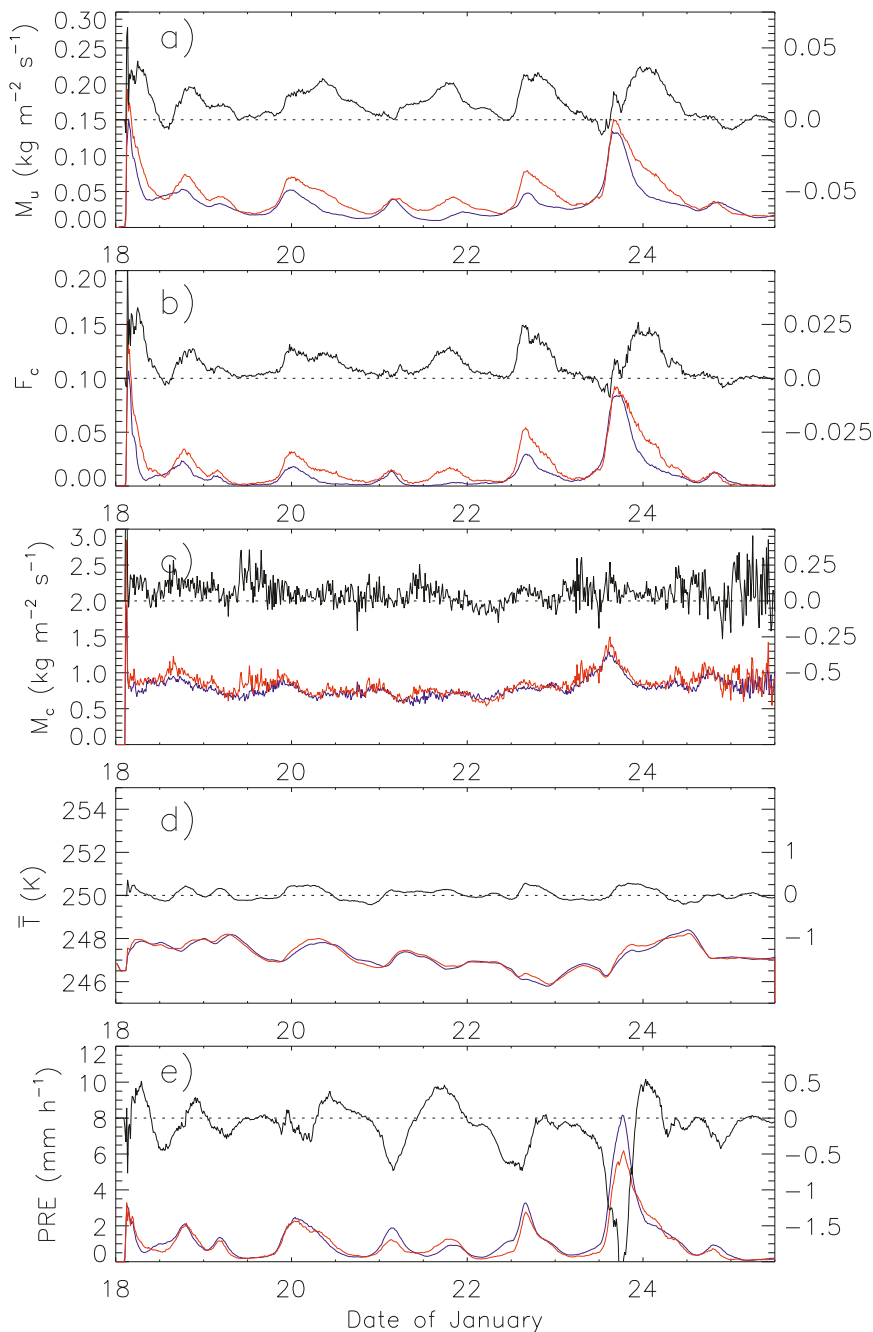


FIG. 8. As in Fig. 1, but for quantities averaged over the perturbed (red) and unperturbed (blue) parts of the 1000-km-domain simulations (PERTP). Black solid lines indicate differences (perturbed minus unperturbed), with black dotted lines included as a reference to show zero difference.

(Fig. 13f). Weaker convection in PERTURBED leads to a further decrease in latent heating (Fig. 13e), which reinforces mean mesoscale descent, low-level drying, and weakening of convection.

In contrast to \bar{T} , there are significant differences in average water vapor mixing ratio between PERTURBED

and UNPERTURBED, as seen by profiles of time-averaged $\overline{\text{RH}}$ in Fig. 9b. This occurs because water vapor must be physically transported from one region to another via the mesoscale circulation and hence has a relatively slow mixing time scale compared to gravity wave adjustment of the temperature field (Grabowski

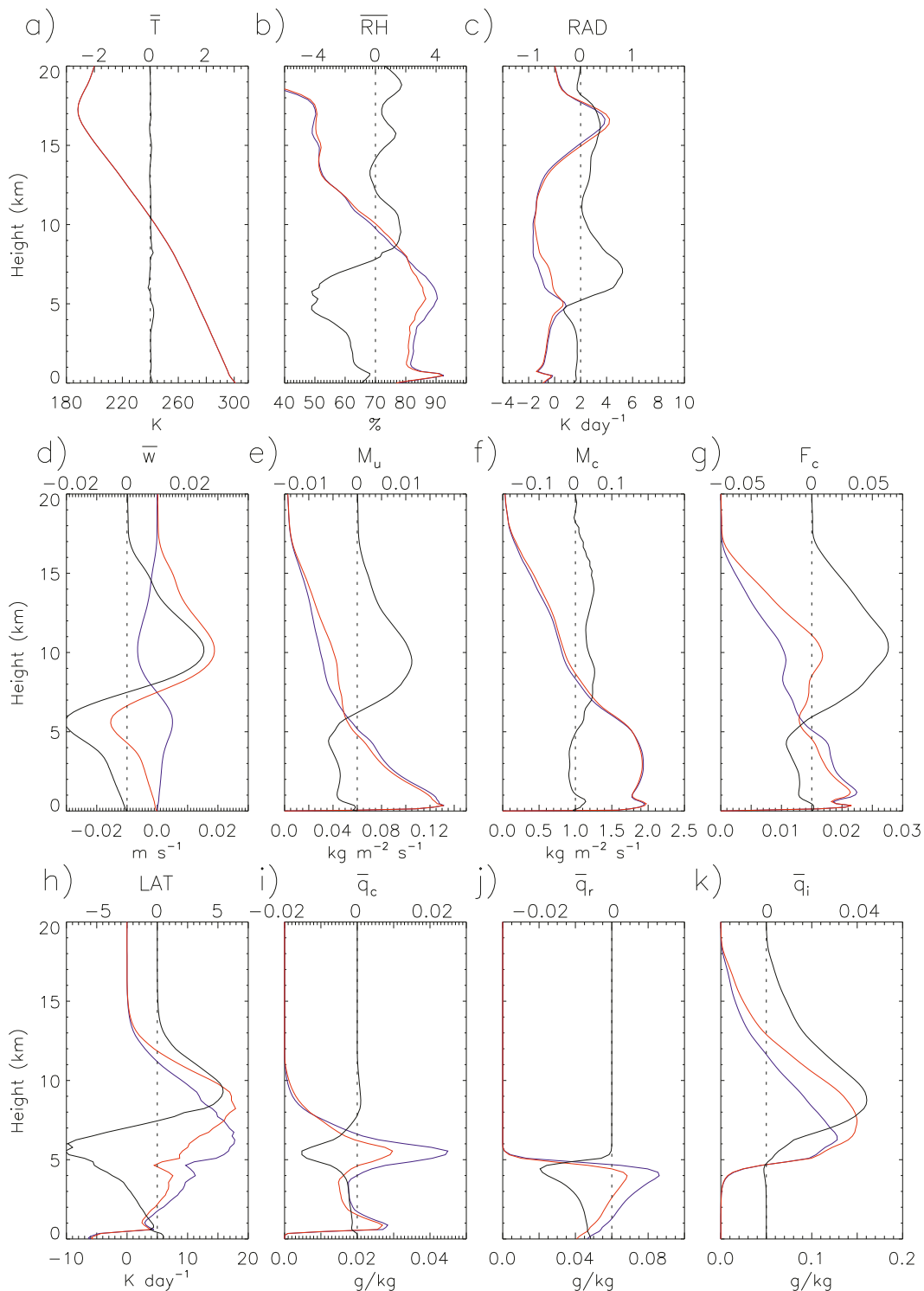


FIG. 9. Vertical profiles of (a) horizontally average temperature, (b) relative humidity, (c) radiative heating rate, (d) vertical velocity, (e) updraft mass flux, (f) convective updraft mass flux, (g) fraction of the domain with convective updrafts, (h) latent heating rate, (i) cloud water mixing ratio, (j) rain mixing ratio, (k) ice mixing ratio, averaged between 1200 UTC 19 Jan and 1200 UTC 25 Jan for the perturbed (red) and unperturbed (blue) parts of the 1000-km-domain simulations (PERTP). Black solid lines indicate differences (perturbed minus unperturbed), with black dotted lines included as a reference to show zero difference.

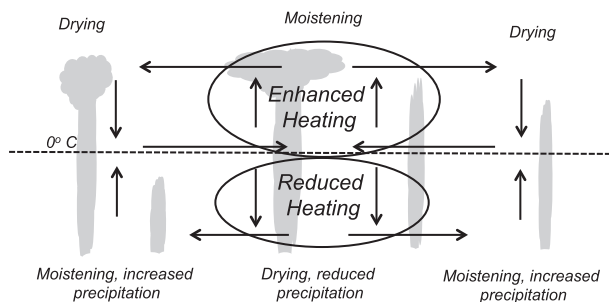


FIG. 10. Schematic diagram of the mesoscale response to localized heating/cooling perturbations.

and Moncrieff 2004). Mean vertical velocities of about 2 cm s^{-1} over a depth of 5 km in the perturbed region (Fig. 9c) suggest a time scale associated with the mesoscale circulation of about 2.5 days. This time scale is consistent with the changes in boundary layer RH and weakening of convection in PERTURBED that occur after about 3 days. It also supports our contention that the weakening of convection at low levels is associated with the mesoscale circulation. Note that there is a small increase of water vapor and, hence, RH above about 8 km in PERTURBED compared to UNPERTURBED (Fig. 9b) associated with mean ascent in PERTURBED. However, this has limited impact on convection since it leads to only a very small increase in virtual temperature of the environment and, hence, stability (there could be some impact on entrainment, but these effects are also expected to be small above 8 km).

Drying caused by mean descent associated with the mesoscale circulation below 8 km in PERTURBED (Fig. 9b) also leads to greater rain evaporation and reduced surface precipitation (Fig. 8). The increased evaporation and reduced F_c at low levels result in smaller cloud water and rain mixing ratios in PERTURBED compared with UNPERTURBED below 5 km (Figs. 9i,j). On the other hand, invigorated convection in PERTURBED at upper levels leads to slightly greater cloud water mixing ratio from about 7.5 to 10 km, as well as substantially larger ice mixing ratios and a higher cloud top (Fig. 9k). Differences in radiative heating are small between PERTURBED and UNPERTURBED (Fig. 9c). However, if polluted conditions lead to enhanced concentrations of ice in anvils and subsequently increased upper-tropospheric radiative heating as simulated by MG11, this could enhance the mesoscale circulations described here. Such an investigation of radiatively driven mesoscale circulations is beyond the scope of this paper but should be explored in future work.

6. Summary and conclusions

In this study, we examined the response of convection to localized heating and cooling perturbations to

specifically test the idea of aerosol-induced convective invigoration proposed by R08 and others. According to this mechanism, aerosol loading leads to a reduction of rain production via collision-coalescence and, subsequently, lofting of cloud water and enhanced freezing and ice processes in updrafts at mid- and upper levels, increasing latent heating and buoyancy. We tested this mechanism by performing different sets of two-dimensional simulations applying localized heating perturbations to updrafts and cooling to downdrafts. The model setup was based on TWP-ICE, with simulations performed for the period from 0000 UTC 18 January to 1200 UTC 25 January 2006, during a period of active monsoon conditions. An ensemble approach (120 or 240 members) was used to improve robustness.

With perturbed heating (cooling) applied to updrafts (downdrafts) throughout the domain, there is an initial invigoration of convection in terms of mean updraft mass flux, convective fraction, and surface precipitation. However, rapid adjustment of the environment limits the impact of these perturbations on convective characteristics after about 24 h. This adjustment is evident by differences in mean temperature profiles between the perturbed and unperturbed simulations, which stabilize the troposphere to the perturbed heating. While there is evidence for many time scales relevant to convective adjustment (Kuang 2010), we propose two processes that may be important to the overall adjustment time scale here: gravity wave dynamics and vertical mixing by convection. The adjustment time scale is nearly independent of perturbation amplitude, which is consistent with adjustment by gravity waves and convective vertical mixing since time scales for these processes are primarily dependent upon mean stability, convective fraction within the domain, and distance between convective cells, which in turn are controlled mostly by the initial and large-scale forcing conditions rather than the perturbations themselves. However, we emphasize that other processes may also be important in controlling the overall adjustment time scale.

Additional simulations tested the impact of applying heating and cooling perturbations to only part of the domain (the inner 250 km of a 1000-km domain). This had two primary effects:

- 1) In the upper troposphere (above 6 km), the applied heating perturbations led to an invigoration of convection in the perturbed region. This in turn led to increased latent heating, but the resulting buoyancy anomalies were rapidly dispersed by gravity waves associated with a mean mesoscale ascent (descent) in the perturbed (unperturbed) region. Thus, there was little stabilization of the environment and

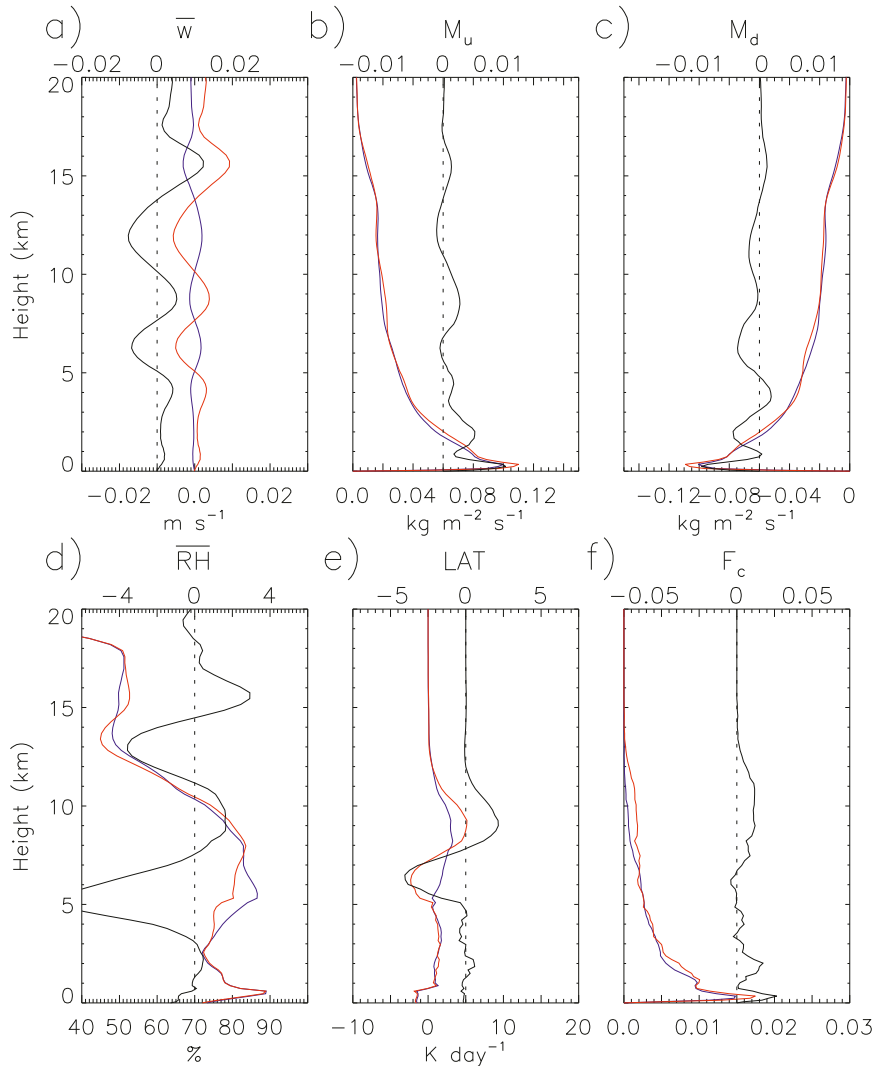


FIG. 11. Vertical profiles of (a) horizontally averaged vertical velocity, (b) updraft mass flux, (c) downdraft mass flux, (d) relative humidity, (e) latent heating rate, and (f) fraction of the domain with convective updrafts, averaged between 0000 UTC 18 Jan and 1200 UTC 19 Jan for the perturbed (red) and unperturbed (blue) parts of the 1000-km-domain simulations (PERTP). Black solid lines indicate differences (perturbed minus unperturbed), with black dotted lines included as a reference to show zero difference.

applied heating perturbations were able to directly drive convective invigoration over the duration of the simulations, unlike simulations in which perturbed conditions were applied across the domain.

- 2) In the lower troposphere (below 6 km), there was also an initial invigoration of convection in the perturbed relative to unperturbed region, but after about 3 days there was a relative weakening of convection within the perturbed region. This occurred because of a decrease in latent heating at midlevels in the perturbed region, leading to mean mesoscale descent below about 7 km. This mesoscale circulation in turn led

to low-level drying and reduced boundary layer moist static energy and, eventually, a weakening of convection.

Overall, these results suggest that the convective invigoration effect caused by localized heating perturbations associated with aerosols cannot be sustained beyond the convective adjustment time scale in a uniform larger-scale environment. However, in the presence of larger-scale heating (aerosol) gradients, invigoration can be sustained over time. The implication is that aerosol invigoration effects via localized heating perturbations in an

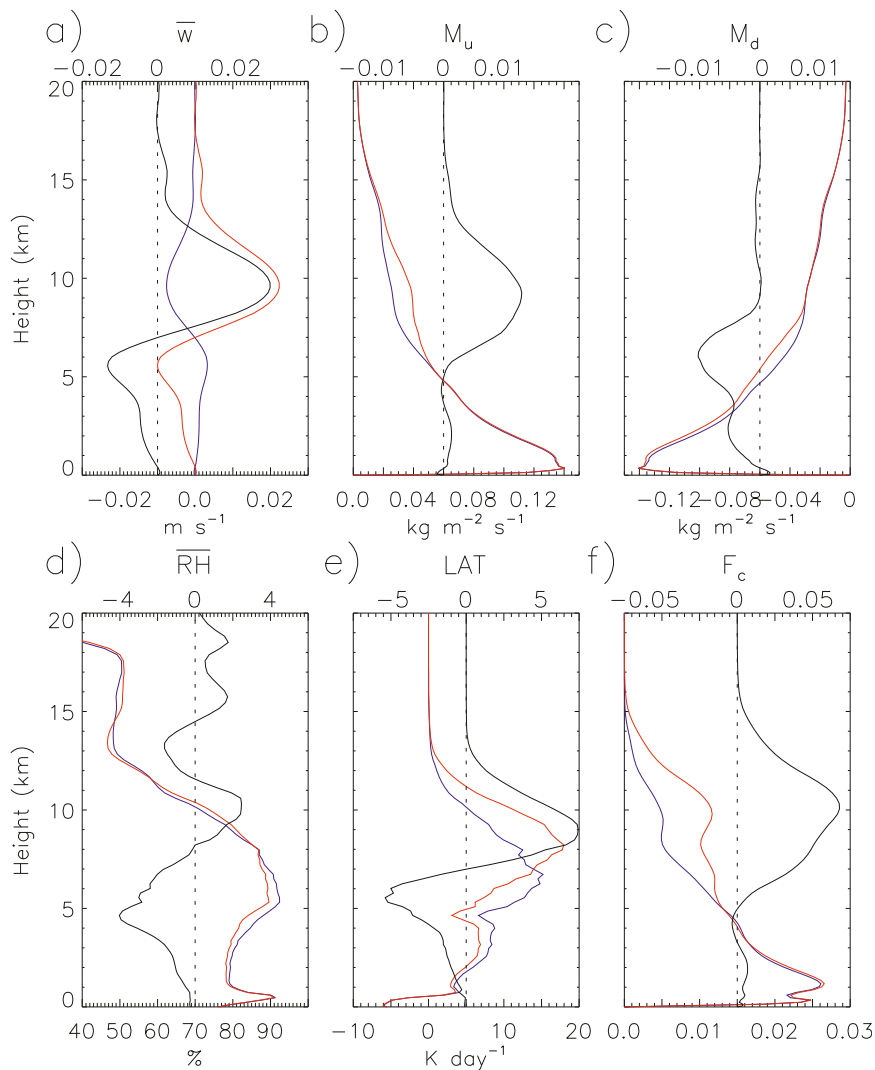


FIG. 12. As in Fig. 11, but averaged between 1200 UTC 19 Jan and 0000 UTC 21 Jan.

initially uniform larger-scale dynamic and thermodynamic environment require larger-scale heating gradients and are closely connected with gravity wave and meso-scale dynamics beyond the convective adjustment time scale (~ 24 h for the mean large-scale conditions here). Our results instead suggest that the invigoration effect is intimately coupled with larger-scale dynamics through a two-way feedback, and in the absence of alterations in the larger-scale circulation there is limited invigoration beyond the convective adjustment time scale. This also suggests the importance of spatial and temporal scales of the heating (aerosol) perturbations relative to pertinent dynamical scales. These dynamical scales differ fundamentally at higher latitudes, since heating anomalies can be retained through balanced circulations there. Moreover, at midlatitudes convection often occurs in a strongly

nonuniform larger-scale dynamic and thermodynamic environment, with convection in a state of nonequilibrium with its environment [i.e., “type 1” convection from Emanuel (1994)]. In type 1 convection, heating perturbations associated with aerosol loading may be expected to have a greater effect on convective characteristics given that convective characteristics are more dependent upon initial conditions (e.g., CAPE, convective inhibition) than the large-scale forcing. This is in contrast to the simulations here, where convection was in near equilibrium with the large-scale forcing [i.e., “type 2” convection from Emanuel (1994)], which is a situation typical of the tropics.

There are several important caveats to this work. First, 2D dynamics were employed for continuity with previous studies of aerosol effects on TWP-ICE convection (Lee and Feingold 2010; MG11; Lee 2012) and

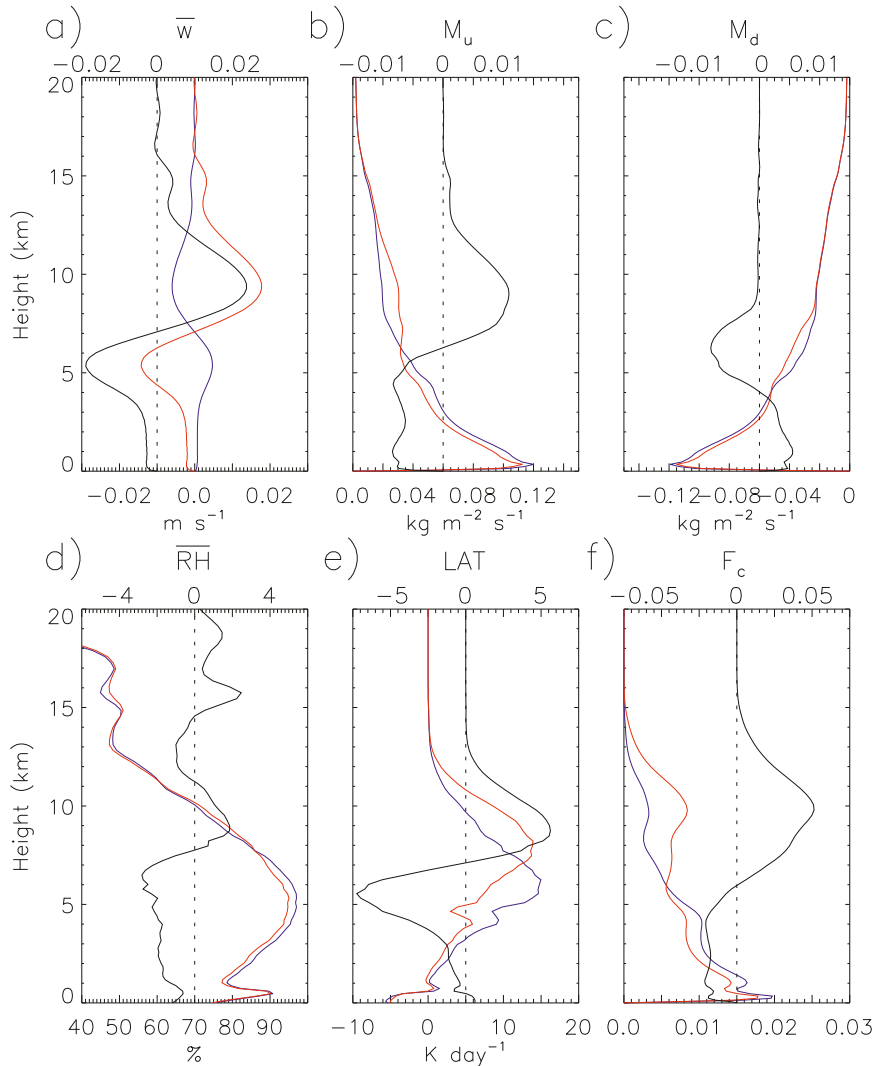


FIG. 13. As in Fig. 11, but averaged between 0000 UTC 21 Jan and 1200 UTC 22 Jan.

convective–radiative equilibrium (G06; GM11; van den Heever et al. 2011), as well as for computational efficiency given the large number of simulations performed. However, it is well known that 3D dynamics differ from 2D, both in terms of convection (e.g., Grabowski et al. 1998; Phillips and Donner 2006; Petch et al. 2008) and coupling of gravity waves with heat sources (Bretherton and Smolarkiewicz 1989). While this may change details of results, we do not expect this to affect the main conclusions. Future work will focus on simulating these effects using 3D dynamical models. We also note that previous work has shown that convective organization differs between 2D and 3D, with subsequent impacts on the mean state (Tompkins 2000). However, the relatively small domain used in our simulations limited the large-scale organization of convection so that this impact of dimensionality is likely to be less important here.

Moreover, Grabowski et al. (1998) showed that 2D and 3D models produced similar results for strongly forced tropical cloud systems similar to the TWP-ICE case simulated here.

This study also neglected feedback between convection and the imposed large-scale forcing, and between convection and surface fluxes; large-scale forcing and surface fluxes were specified identically in all simulations. This simplification allowed us to examine feedbacks between convection and the larger-scale environment in a framework with realistic time-dependent forcing, but without complications due to feedbacks with the large-scale forcing and the surface. In future work we plan to investigate the impact of feedbacks between convection and large-scale forcing in the context of indirect aerosol effects using both idealized and realistic model configurations.

Acknowledgments. This work was partially supported by the U.S. DOE ASR DE-SC0008648, U.S. DOE ASR DE-SC0005336, subawarded through NASA NNX12AH90G, and the NSF Science and Technology Center for Multiscale Modeling of Atmospheric Processes (CMMAP), managed by Colorado State University under Cooperative Agreement ATM-0425247. We thank Z. Piotrowski for help setting up the ensemble simulations.

REFERENCES

- Allen, G., and Coauthors, 2008: Aerosol and trace-gas measurements in the Darwin area during the wet season. *J. Geophys. Res.*, **113**, D06306, doi:10.1029/2007JD008706.
- Bretherton, C. S., and P. Smolarkiewicz, 1989: Gravity waves, compensating subsidence, and detrainment around cumulus clouds. *J. Atmos. Sci.*, **46**, 740–759.
- Cohen, B. G., and C. G. Craig, 2004: The response time of a convective cloud ensemble to a change in forcing. *Quart. J. Roy. Meteor. Soc.*, **130**, 933–944.
- Ekman, A. M. L., A. Engstrom, and A. Soderberg, 2011: Impact of two-way aerosol–cloud interaction and changes in aerosol size distribution on simulated aerosol-induced deep convective cloud sensitivity. *J. Atmos. Sci.*, **68**, 685–697.
- Emanuel, K. A., 1994: *Atmospheric Convection*. Oxford University Press, 580 pp.
- Fan, J., and Coauthors, 2009: Dominant role by vertical wind shear in regulating aerosol effects on deep convective clouds. *J. Geophys. Res.*, **114**, D22206, doi:10.1029/2009JD012352.
- , L. R. Leung, Z. Li, H. Morrison, Y. Qian, Y. Zhou, and H. Chen, 2012a: Aerosol impacts on clouds and precipitation in southeast China: Results from bin and bulk microphysics. *J. Geophys. Res.*, **117**, D00K36, doi:10.1029/2011JD016537.
- , D. Rosenfeld, Y. Ding, L. R. Leung, and Z. Li, 2012b: Potential aerosol indirect effects on atmospheric circulation and radiative forcing through deep convection. *Geophys. Res. Lett.*, **39**, L09806, doi:10.1029/2012GL051851.
- Fridlind, A. M., and Coauthors, 2012: A comparison of TWP-ICE observational data with cloud-resolving model results. *J. Geophys. Res.*, **117**, D05204, doi:10.1029/2011JD016595.
- Grabowski, W. W., 2001: Coupling cloud processes with the large-scale dynamics using the Cloud-Resolving Convection Parameterization (CPRP). *J. Atmos. Sci.*, **58**, 978–997.
- , 2004: An improved framework for superparameterization. *J. Atmos. Sci.*, **61**, 1940–1952.
- , 2006: Indirect impact of atmospheric aerosols in idealized simulations of convective–radiative quasi equilibrium. *J. Climate*, **19**, 4664–4682.
- , and P. K. Smolarkiewicz, 1999: CRCP: A cloud resolving convection parameterization for modeling the tropical convecting atmosphere. *Physica D*, **133**, 171–178.
- , and M. W. Moncrieff, 2004: Moisture-convection feedback in the tropics. *Quart. J. Roy. Meteor. Soc.*, **130**, 3081–3104.
- , and H. Morrison, 2011: Impact of atmospheric aerosols in simulations of convective–radiative quasi equilibrium: Double-moment microphysics. *J. Climate*, **24**, 1897–1912.
- , X. Wu, M. W. Moncrieff, and W. D. Hall, 1998: Cloud-resolving modeling of cloud systems during phase III of GATE. Part II: Effects of resolution and the third spatial dimension. *J. Atmos. Sci.*, **55**, 3264–3282.
- Khain, A. P., and B. Lynn, 2009: Simulation of a supercell storm in clean and dirty atmosphere using weather research and forecast model with spectral bin microphysics. *J. Geophys. Res.*, **114**, D19209, doi:10.1029/2009JD011827.
- , D. Rosenfeld, and A. Pokrovsky, 2005: Aerosol impact on the dynamics and microphysics of deep convective clouds. *Quart. J. Roy. Meteor. Soc.*, **131**, 2639–2663.
- Kiehl, J. T., J. J. Hack, and B. P. Briegleb, 1994: The simulated earth radiation budget of the National Center for Atmospheric Research community climate model CCM2 and comparisons with the Earth Radiation Budget Experiment (ERBE). *J. Geophys. Res.*, **99** (D10), 20 815–20 827.
- Koren, I., Y. J. Kaufman, D. Rosenfeld, L. A. Remer, and Y. Rudich, 2005: Aerosol invigoration and restructuring of Atlantic convective clouds. *Geophys. Res. Lett.*, **32**, L14828, doi:10.1029/2005GL0232187.
- Kuang, Z., 2010: Linear response functions of a cumulus ensemble to temperature and moisture perturbations and implications for the dynamics of convective coupled waves. *J. Atmos. Sci.*, **67**, 941–962.
- Lebo, Z. J., and J. H. Seinfeld, 2011: Theoretical basis for convective invigoration due to increased aerosol concentration. *Atmos. Chem. Phys.*, **11**, 5407–5429.
- Lee, S.-S., 2012: Effect of aerosol on circulations and precipitation in deep convective clouds. *J. Atmos. Sci.*, **69**, 1957–1974.
- , and G. Feingold, 2010: Precipitating cloud-system response to aerosol perturbations. *Geophys. Res. Lett.*, **37**, L23806, doi:10.1029/2010GL045596.
- , L. J. Donner, V. T. J. Phillips, and Y. Ming, 2008: Examination of aerosol effects on precipitation in deep convective clouds during the 1997 ARM summer experiment. *Quart. J. Roy. Meteor. Soc.*, **134**, 1201–1220.
- , G. Feingold, and P. Y. Chuang, 2012: Effect of aerosol on cloud–environmental interactions in trade cumulus. *J. Atmos. Sci.*, **69**, 3607–3632.
- Mapes, B. E., 2004: Sensitivities of cumulus-ensemble rainfall in a cloud-resolving model with parameterized large-scale dynamics. *J. Atmos. Sci.*, **61**, 2308–2317.
- May, P. T., J. H. Mather, G. Vaughan, and C. Jakob, 2008: Characterizing oceanic convective cloud systems: The Tropical Warm Pool International Cloud Experiment. *Bull. Amer. Meteor. Soc.*, **89**, 153–155.
- Morrison, H., 2012: On the robustness of aerosols effects on an idealized supercell storm simulated using a cloud system-resolving model. *Atmos. Chem. Phys.*, **12**, 7689–7705, doi:10.5194/acp-12-7689-2012.
- , and W. W. Grabowski, 2007: Comparison of bulk and bin warm rain microphysics models using a kinematic framework. *J. Atmos. Sci.*, **64**, 2839–2861.
- , and —, 2008a: Modeling supersaturation and subgrid-scale mixing with two-moment warm bulk microphysics. *J. Atmos. Sci.*, **65**, 792–812.
- , and —, 2008b: A novel approach for representing ice microphysics in models: Description and tests using a kinematic framework. *J. Atmos. Sci.*, **65**, 1528–1548.
- , and —, 2011: Cloud-system resolving model simulations of aerosol indirect effects on tropical deep convection and its thermodynamic environment. *Atmos. Chem. Phys.*, **11**, 10 503–10 523, doi:10.5194/acp-11-10503-2011.
- Nie, J., and Z. Kuang, 2012: Response of shallow cumulus convection to large-scale temperature and moisture perturbations: A comparison of large-eddy simulations and a convective parameterization based on stochastically entraining parcels. *J. Atmos. Sci.*, **69**, 1936–1956.

- Petch, J. C., P. N. Blossey, and C. S. Bretherton, 2008: Differences in the lower troposphere in two- and three-dimensional cloud-resolving model simulations of deep convection. *Quart. J. Roy. Meteor. Soc.*, **134**, 1941–1946.
- Phillips, V. T. J., and L. J. Donner, 2006: Cloud microphysics, radiation, and vertical velocities in two- and three-dimensional simulations of deep convection. *Quart. J. Roy. Meteor. Soc.*, **132**, 3011–3033.
- Rosenfeld, D., U. Lohmann, G. B. Raga, C. D. O’Dowd, M. Kulmala, S. Fuzzi, A. Reissell, and M. O. Andreae, 2008: Flood or drought: How do aerosols affect precipitation? *Science*, **321**, 1309–1313.
- Seifert, A., and K. D. Beheng, 2006: A two-moment cloud microphysics parameterization for mixed-phase clouds. Part 2: Maritime vs. continental deep convective storms. *Meteor. Atmos. Phys.*, **92**, 45–66.
- , C. Kohler, and K. Beheng, 2012: Aerosol-cloud-precipitation effects over Germany as simulated by a convective-scale numerical weather prediction model. *Atmos. Chem. Phys.*, **12**, 709–715.
- Storer, R. L., and S. C. van den Heever, 2013: Microphysical processes evident in aerosol forcing of tropical deep convective clouds. *J. Atmos. Sci.*, **70**, 430–446.
- Tan, Z.-M., F. Zhang, R. Rotunno, and C. Snyder, 2004: Mesoscale predictability of moist baroclinic waves: Experiments with parameterized convection. *J. Atmos. Sci.*, **61**, 1794–1804.
- Tao, W.-K., X. Li, A. Khain, T. Matsui, S. Lang, and J. Simpson, 2007: Role of atmospheric aerosol concentration on deep convective precipitation: Cloud-resolving model simulations. *J. Geophys. Res.*, **112**, D24S18, doi:10.1029/2007JD008728.
- , J.-P. Chen, Z. Li, C. Wang, and C. Zhang, 2012: Impact of aerosols on convective clouds and precipitation. *Rev. Geophys.*, **50**, RG2001, doi:10.1029/2011RG000369.
- Tompkins, A. M., 2000: The impact of dimensionality on long-term cloud-resolving model simulations. *Mon. Wea. Rev.*, **128**, 1521–1535.
- , and G. C. Craig, 1998: Time-scales of adjustment to radiative-convective equilibrium in the tropical atmosphere. *Quart. J. Roy. Meteor. Soc.*, **124**, 2693–2713.
- Troen, I., and L. Mahrt, 1986: A simple model of the atmospheric boundary layer: Sensitivity to surface evaporation. *Bound.-Layer Meteor.*, **37**, 129–148.
- Tulich, S. N., and B. E. Mapes, 2010: Transient environmental sensitivities of explicitly simulated tropical convection. *J. Atmos. Sci.*, **67**, 923–940.
- van den Heever, S. C., G. G. Carrio, W. R. Cotton, P. J. DeMott, and A. J. Prenni, 2006: Impacts of nucleating aerosol on Florida storms. Part I: Mesoscale simulations. *J. Atmos. Sci.*, **63**, 1752–1775.
- , G. L. Stephens, and N. B. Wood, 2011: Aerosol indirect effects on tropical convective characteristics under conditions of radiative-convective equilibrium. *J. Atmos. Sci.*, **68**, 699–718.
- Xie, S., T. Hume, C. Jakob, S. A. Klein, R. McCoy, and M. Zhang, 2010: Observed large-scale structures and diabatic heating and drying profiles during TWP-ICE. *J. Climate*, **23**, 57–79.
- Zhang, F., N. Bei, R. Rotunno, C. Snyder, and C. C. Epifanio, 2007: Mesoscale predictability of moist baroclinic waves: Convection-permitting experiments and multistage error growth dynamics. *J. Atmos. Sci.*, **64**, 3579–3594.